

Topology-Dependent Phase Classification of Effective Potentials in Einstein–Cartan + Nieh–Yan Minisuperspace

Muacca

January 11, 2026

Abstract

We study Einstein–Cartan (EC) gravity supplemented with the Nieh–Yan (NY) term in a Euclidean-signature minisuperspace framework, and classify the resulting effective potential into distinct “phases.” Based on the presence or absence of local minima and barriers in the effective potential, we define three types: (I) metastable well with barrier, (II) barrier-free rolling, and (III) unstable/boundary-attached configurations.

While the Nieh–Yan density (a 4-form) can be written as an exact derivative, it is geometrically defined through the coframe and torsion. To facilitate meaningful comparison, we evaluate topology dependence under a unified ansatz. We adopt spatial sections that admit left-invariant coframes, enabling systematic description within a common minisuperspace framework.

As concrete test beds, we consider: (i) S^3 , (ii) T^3 , and (iii) Nil^3 . For the NY term, we focus on the complete form (FULL) as the primary object, while also examining TT (torsion-torsion component only) and REE (the remaining component) as diagnostic comparisons to disentangle the contributions within FULL.

Our investigation addresses two main questions: (1) How does the phase (Type I/II/III) of the effective potential depend on topology? (2) Can we identify, through numerical scanning, critical conditions corresponding to well formation/disappearance and barrier collapse, and organize their geometric dependence?

Our scanning results suggest the following:

- The phase structure of the effective potential varies systematically with topology.
- Within the NY term, some contributions exhibit relative insensitivity to topology, while others appear selectively depending on geometric conditions.

1 Introduction

1.1 Background: Correspondence Between Geometric Input and Phase Structure of Effective Potentials

In theories where the coframe and connection are treated as independent variables, curvature and torsion are introduced on equal footing as geometric degrees of freedom. In particular, Einstein–Cartan (EC) theory and its extensions allow torsion and topological densities to appear in the action, potentially making the structure of the reduced effective theory sensitive to geometric input.

Meanwhile, minisuperspace reduction based on symmetry assumptions provides a powerful procedure for mapping infinite-dimensional field theories to finite-dimensional systems. However, even within the same reduction framework, how differences in spatial topology or structure constants of homogeneous spaces affect the shape of the effective potential $V_{\text{eff}}(r)$ —including the presence or absence of minima and barriers, and transitions to rolling behavior—has not been systematically organized.

For this reason, it is important to classify and visualize, in a reproducible manner, the correspondence between geometric input and the phase structure of the reduced effective potential. This work organizes this correspondence using representative homogeneous spaces as test beds, presenting the results as phase diagrams and representative points.

1.2 Our Approach: Treating EC+NY as a “Phase Classification Problem for Effective Potentials”

In this work, we take EC+NY (Einstein–Cartan gravity with the Nieh–Yan term) as our object of study and classify the phases of the effective potential in a Euclidean-signature minisuperspace from the perspective of topology dependence. In EC theory, torsion is naturally introduced as geometry, and while the NY density (a 4-form) can be written as an exact derivative, it is geometrically defined through the coframe and torsion. Therefore, by comparing how the effective potential changes when varying the spatial topology under the same minisuperspace ansatz, we diagnose the phase structure provided by EC+NY from the viewpoint of geometric input.

Although EC+NY originates as a gravitational theory, the focus of this paper is on systematically organizing the influence of geometric input (topology, structure constants, torsion, and NY contributions) on the phase structure after reduction.

1.3 Scope: Three Homogeneous Spaces as Test Beds

To enable comparison from the perspective of topology dependence, we adopt spatial sections that possess homogeneity and can be uniformly described using left-invariant coframes. Specifically, as three representative examples with contrasting properties in structure constants and curvature, we adopt:

- (i) S^3 ($SU(2)$; isotropic positive curvature),
- (ii) T^3 (flat),
- (iii) Nil^3 (compact quotient of the Heisenberg group; anisotropic geometry).

These serve as a minimal set for comparing how “geometric data (structure constants, curvature characteristics)” affect the phase structure of the effective potential under the same reduction procedure.

1.4 Deliverables: Type Classification, Critical Conditions, Phase Diagrams, and Representative Points

The central output of this work is an operational classification based on the shape of $V_{\text{eff}}(r)$. Specifically, we introduce three types:

- (I) Metastable well with barrier,
- (II) Barrier-free rolling,
- (III) Unstable/boundary-attached,

and visualize how these are arranged in parameter space for each topology as phase diagrams. Furthermore, we identify critical conditions corresponding to well formation/disappearance and barrier collapse through numerical scanning, and organize their geometric dependence.

For the NY term, we take the complete form (FULL) as the primary object, while also using TT and REE as diagnostic comparisons to disentangle the contributions (definitions in Sec. 2). Note that TT/REE are not proposed as independent fundamental theories but serve as auxiliary comparisons for understanding the effects of FULL.

Through this approach, we provide a reproducible diagnostic pipeline that returns the phase (Type I/II/III) and critical boundaries of $V_{\text{eff}}(r)$ for given geometric input (topology, parameters). The resulting phase diagrams, representative points, and critical conditions can be used as foundational data for explicitly incorporating topology dependence in EC+NY minisuperspace analysis.

1.5 Paper Organization

The organization of this paper is as follows. Section 2 summarizes the formulation of EC+NY and minisuperspace reduction, as well as the definitions and numerical criteria for Type I/II/III. Section 3 presents the reduction results for S^3 , T^3 , and Nil^3 , showing the form of the effective potential. Section 4 presents numerical scanning results as phase diagrams. Section 5 interprets the phase diagram features based on the analytical structure of the effective potential. Section 6 summarizes representative points and stability metrics (minimum position, barrier height, etc.). Section 7 discusses geometric interpretation and the utility of this framework. Section 8 presents conclusions and future prospects.

1.6 Scope and Limitations

This work focuses on phase classification of effective potentials based on minisuperspace reduction. The following items are outside the scope of this paper and are discussed as future research directions in Sec. 8.

Dynamical evolution: We do not treat time evolution including Friedmann-type constraint equations, nor quantitative calculations of tunneling rates via WKB approximation. The distinction between Type I/II is an operational classification based on the shape of $V_{\text{eff}}(r)$ and does not provide actual transition probabilities.

Quantum corrections: We do not consider quantum corrections at one-loop or higher, nor renormalization group running of coupling constants. The results of this work are based on the classical (tree-level) effective potential.

Matter field coupling: We do not include interactions with matter fields such as spinor or scalar fields. We focus on the geometric structure of pure EC+NY theory.

Inhomogeneous perturbations: We do not analyze inhomogeneous fluctuations beyond the minisuperspace ansatz (spatial homogeneity). Consequently, our results are limited to the homogeneous sector.

Analytic continuation to Lorentzian signature: This work performs calculations in Euclidean signature $(+, +, +, +)$. Wick rotation to Lorentzian signature $(-, +, +, +)$ and interpretation in real-time cosmology are not discussed in detail in this paper.

2 Setup and Conventions

This section summarizes the formulation of EC+NY used in this paper, the premises of minisuperspace reduction, parameters and notation, and the classification conventions (Type I/II/III) for numerical scanning. The main results of this paper (phase diagrams, classification tables, representative points) are obtained based on the conventions defined here.

2.1 Basic Variables and Notation for EC+NY

This paper treats Einstein–Cartan theory (with Euclidean signature) in the first-order formalism (coframe/connection). The basic variables are the coframe (tetrad 1-form) $\{e^a\}$ and the independent spin connection ω^{ab} . The torsion 2-form T^a and curvature 2-form R^{ab} are defined as

$$T^a := de^a + \omega^a{}_b \wedge e^b, \quad (1)$$

$$R^{ab} := d\omega^{ab} + \omega^a{}_c \wedge \omega^{cb}. \quad (2)$$

EC connection and contortion: The Einstein–Cartan connection $\Gamma_{\text{EC},bc}^a$ is expressed as the sum of the Levi–Civita connection $\Gamma_{\text{LC},bc}^a$ and the contortion $K^a{}_{bc}$:

$$\Gamma_{\text{EC},bc}^a = \Gamma_{\text{LC},bc}^a + K^a{}_{bc}. \quad (3)$$

The contortion is determined from torsion as follows (following the convention of Hehl et al. [1]):

$$K_{abc} = \frac{1}{2} (T_{abc} + T_{bca} - T_{cab}). \quad (4)$$

Here all indices are written in lowered form.

Sign conventions: This paper adopts the following conventions:

- Frame metric: $\eta_{ab} = \text{diag}(+1, +1, +1, +1)$ (Euclidean signature)
- Riemann tensor (antisymmetric in 3rd and 4th indices):

$$R^a{}_{bcd} = \partial_c \Gamma^a{}_{bd} - \partial_d \Gamma^a{}_{bc} + \Gamma^a{}_{ec} \Gamma^e{}_{bd} - \Gamma^a{}_{ed} \Gamma^e{}_{bc} \quad (5)$$

- Contortion: Following Hehl et al. [1], $K_{abc} = \frac{1}{2}(T_{abc} + T_{bca} - T_{cab})$
- Levi–Civita symbol: $\varepsilon_{0123} = +1$

Remark on index labels. All internal indices a, b, \dots are *Euclidean* frame labels. In particular, the label $a = 0$ does *not* denote Lorentzian time in this paper; it is simply

one of the orthonormal directions on the homogeneous spatial section. The S^1 direction is labeled $a = 3$.

Hereafter, the wedge product is written as \wedge . Details of index conventions (distinction between internal indices a, b, \dots and coordinate indices) and supplementary derivations are summarized in Appendix A.

2.2 Nieh–Yan Density and Nieh–Yan Term

The Nieh–Yan density (4-form) N is a geometric quantity defined using the coframe and torsion, expressed as an exact derivative:

$$N = d(e^a \wedge T_a). \quad (6)$$

The “Nieh–Yan (NY) term” in this paper refers to the contribution $\theta_{\text{NY}} N$ in the action, where θ_{NY} is a coupling constant.

In differential-form notation, the Nieh–Yan 4-form satisfies the identity

$$N = d(e^a \wedge T_a) = T^a \wedge T_a - e^a \wedge e^b \wedge R_{ab}, \quad (7)$$

which holds for an arbitrary coframe e^a and independent connection ω^{ab} . For a constant coupling θ_{NY} on a compact manifold without boundary, $\int N$ is a boundary term and does not modify the bulk Euler–Lagrange equations. In minisuperspace reduction, however, the NY term can shift the reduced Euclidean action between homogeneous configurations once boundary conditions along the S^1 direction are specified. Throughout this paper, we therefore treat $\theta_{\text{NY}} N$ as part of the reduced action density defining the effective potential, while noting its boundary-term character in the full 4D theory.

Component decomposition of NY density: In frame basis calculations, the NY density decomposes into two contributions:

$$N = N_{\text{TT}} - N_{\text{REE}}, \quad (8)$$

where:

- N_{TT} : Torsion-torsion term, taking the form $\frac{1}{4}\varepsilon^{abcd}T^e{}_{ab}T_{ecd}$.
- N_{REE} : Riemann-torsion term, taking the form $\frac{1}{4}\varepsilon^{abcd}R_{abcd}$ (curvature from EC connection).

In this paper, we take the complete NY density **FULL** as the primary object, while also using **TT** (N_{TT} only) and **REE** (N_{REE} only) as diagnostic comparisons.

We emphasize that N_{TT} and N_{REE} are *diagnostic* pieces corresponding to the two terms in Eq. (7):

$$N_{\text{TT}} := T^a \wedge T_a, \quad N_{\text{REE}} := e^a \wedge e^b \wedge R_{ab}, \quad N = N_{\text{TT}} - N_{\text{REE}}. \quad (9)$$

These are introduced to disentangle contributions within FULL, not as independent fundamental theories.

Note on exact derivative property: The fact that the NY density can be written as an exact derivative implies that its integral over a closed manifold may become a topological invariant. However, in minisuperspace reduction, the boundary term contribution can become non-trivial due to the symmetry of the ansatz. Within the scope of this work, we operationally classify the influence on the phase structure of $V_{\text{eff}}(r)$ obtained through reduction.

2.3 Minisuperspace Reduction

2.3.1 Basic strategy of reduction

The minisuperspace reduction in this paper is a procedure that substitutes an ansatz assuming spatial homogeneity into the action and reduces it to an effective action with finite degrees of freedom through spatial integration.

Specifically, we decompose the 4-dimensional Euclidean manifold as $\mathcal{M}_4 = \mathcal{M}_3 \times S^1$, adopting a compact quotient of a 3-dimensional Lie group admitting left-invariant coframes for \mathcal{M}_3 . Let L denote the circumference in the S^1 direction, and characterize the “size” of \mathcal{M}_3 by a single scale parameter r .

With this setup, the field degrees of freedom are reduced to the following finite number of parameters:

- Spatial scale variable r (argument of the effective potential $V_{\text{eff}}(r)$)
- A finite number of parameters specifying torsion amplitude (see Sec. 2.3.3)

2.3.2 Coframe and structure constants

We introduce left-invariant coframes $\{\sigma^i\}$ ($i = 0, 1, 2$) on the 3-dimensional space \mathcal{M}_3 and construct the 4-dimensional coframe as

$$\begin{aligned} e^a &= r \sigma^i \quad (a = i = 0, 1, 2), \\ e^a &= L d\tau \quad (a = 3), \end{aligned} \quad (10)$$

where $\tau \in [0, 1]$ is the periodic coordinate in the S^1 direction.

The left-invariant coframes satisfy the Maurer–Cartan structure equation

$$d\sigma^i = -\frac{1}{2} C^i_{jk} \sigma^j \wedge \sigma^k. \quad (11)$$

The structure constants C^i_{jk} characterize the geometry of \mathcal{M}_3 and take the following values for the three test beds treated in this paper:

Table 1: Structure constants and background Ricci scalar for each topology.

Topology	Structure constants	Background Ricci scalar R_{LC}
S^3 (SU(2))	$C^i_{jk} = \frac{4}{r} \varepsilon_{ijk}$	$+24/r^2$ (positive curvature)
T^3 (Abelian)	$C^i_{jk} = 0$	0 (flat)
Nil ³ (Heisenberg)	$C^2_{01} = -1/r, C^2_{10} = +1/r, \text{others } 0$	$-1/(2r^2)$ (negative curvature)

Here ε_{ijk} is the 3-dimensional Levi–Civita symbol.

Note that the r -dependence of the structure constants results from adopting the orthonormal frame $e^a = r \sigma^a$. Here σ^a is the left-invariant coframe of “unit size,” and rescaling by the physical scale r introduces the $1/r$ factor in the structure constants.

2.3.3 Torsion ansatz: Parametrization based on irreducible decomposition

In Einstein–Cartan theory, the torsion tensor T^a_{bc} is a geometric degree of freedom independent of the coframe. Following the irreducible decomposition of torsion in 4 dimensions (Hehl et al. [1]), we introduce the following two components:

T1 component (totally antisymmetric / Axial): As totally antisymmetric torsion in the spatial directions, we adopt

$$T^{(1)}_{abc} = \frac{2\eta}{r} \varepsilon_{abc} \quad (a, b, c \in \{0, 1, 2\}). \quad (12)$$

Here η is a dimensionless parameter, scanned including its sign.

This component corresponds to the pseudovector (axial vector) part of torsion $S^\mu = \varepsilon^{\mu\nu\rho\sigma} T_{\nu\rho\sigma}$, with S^3 taking a nonzero value.

T2 component (vector trace): Using a vector $V_\mu = (0, 0, 0, V)$ along the S^1 direction, we adopt

$$T^{(2)}_{abc} = \frac{1}{3} (\eta_{ac} V_b - \eta_{ab} V_c). \quad (13)$$

Here $V > 0$ is a positive-valued parameter, and η_{ab} is the frame metric (in this paper, δ_{ab}).

This component corresponds to the vector trace part of torsion $T_\mu = T^\lambda_{\mu\lambda}$.

Mode definitions: By combining T1 and T2, we define the following three computational modes:

Table 2: Torsion mode definitions.

Mode	T1 (Axial)	T2 (Vector)	Independent parameters
AX	✓	—	η
VT	—	✓	V
MX	✓	✓	η, V

The main results of this paper are based on MX mode (mixed). AX and VT modes are used for diagnostic purposes to disentangle the contribution of each torsion component.

2.4 Parameters and Scanning Variables

2.4.1 Parameter list

The main parameters used in this paper are summarized below:

Geometric parameters:

- r : Spatial scale variable. Argument of $V_{\text{eff}}(r)$, scanned over $r > 0$.
- L : Circumference in the S^1 direction. Fixed at $L = 1$ in this paper.

Torsion parameters:

- η : Axial torsion amplitude. Scanned over $\eta \in [-10, 5]$ including sign.
- V : Vector torsion amplitude. Scanned over $V \in [0, 5]$.

Coupling constants:

- κ : Gravitational coupling constant. Fixed at $\kappa = 1$ in this paper.
- θ_{NY} : Nieh–Yan coupling. Scanned over $\theta_{\text{NY}} \in [0, 5]$. For $\theta_{\text{NY}} < 0$, the sign of the B term (r^2 coefficient) in the effective potential is reversed, and the phase structure is mirrored in the η direction, so it can be inferred from results in the positive range.

2.4.2 Scanning strategy

For phase diagram generation, we primarily visualize slices of the (V, η) plane for representative values of θ_{NY} (e.g., $\theta_{\text{NY}} = 0, 1, 2$).

For each parameter point, we search for extrema of $V_{\text{eff}}(r)$ in the allowed region $[r_{\min}, r_{\max}] = [0.01, 10^6]$ and determine the Type I/II/III classification (Sec. 2.6).

2.4.3 Note on dimensional analysis

Since we fix $\kappa = L = 1$, all quantities are dimensionless. To restore physical units, r is measured in units of the Planck length $\ell_P = \sqrt{\hbar G/c^3}$, and V_{eff} in units of $\hbar c/\ell_P$. However, the focus of this paper is on phase structure classification, and we do not discuss absolute scales.

2.5 Definition of Effective Potential and “Static Points”

In this work, we define the effective potential $V_{\text{eff}}(r)$ for r from the effective action S_{eff} obtained through reduction as follows.

Derivation procedure:

1. Substitute the ansatz from Sec. 2.3 into the EC+NY action
2. Perform spatial integration to obtain effective action $S_{\text{eff}}[r]$ depending only on r
3. Define the effective potential as $V_{\text{eff}}(r) := -S_{\text{eff}}[r]$

With this sign convention, minima of $V_{\text{eff}}(r)$ correspond to maxima of the action (dominant contributions in the Euclidean path integral).

Definition of static points: Points $r = r_0$ satisfying the extremum condition

$$\frac{dV_{\text{eff}}}{dr} = 0 \tag{14}$$

are called “static points.” Furthermore, if

$$\left. \frac{d^2V_{\text{eff}}}{dr^2} \right|_{r=r_0} > 0 \tag{15}$$

is satisfied, r_0 is a local minimum and represents a stable static point.

Hereafter, we operationally classify phases (Types) based on the shape of $V_{\text{eff}}(r)$ (extrema and barriers).

2.6 Type I/II/III: Operational Definition of Phases

In this paper, we define the following three types based on the shape of $V_{\text{eff}}(r)$. “Phase” is a convenient expression and refers to operational classification, not thermodynamic phase transitions. Figure 1 shows the potential shapes for each phase.

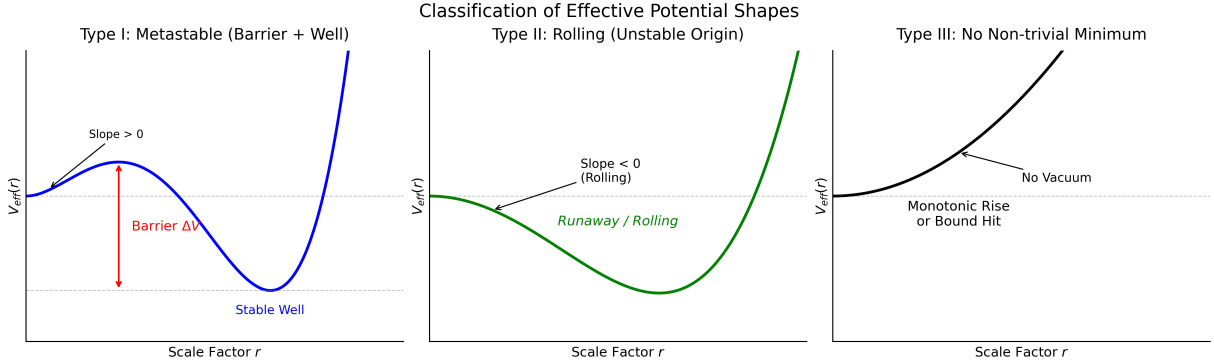


Figure 1: Schematic illustration of Type I/II/III classification based on effective potential shape.

Type I: Metastable well with barrier

- $V_{\text{eff}}(r)$ has a local minimum r_0 within the allowed region
- In the $r \rightarrow 0$ direction, there exists a region where $V_{\text{eff}}(r)$ takes values larger than $V_{\text{eff}}(r_0)$ (barrier)
- Numerical criterion: Difference $\Delta V > 0$ between V_{eff} at r_0 and maximum value for $r < r_0$

Type II: Rolling (no barrier)

- $V_{\text{eff}}(r)$ has a local minimum r_0 within the allowed region
- However, no barrier exists in the $r \rightarrow 0$ direction ($\Delta V \approx 0$ or V_{eff} monotonically decreasing)
- Numerical criterion: $dV_{\text{eff}}/dr|_{r \rightarrow 0^+} < 0$ (downward slope near origin)

Type III: Unstable / boundary-attached

- No stable local minimum exists within the allowed region
- Typical examples:
 - Extremum search reaches r_{\min} or r_{\max} (bound hit)
 - Curvature condition $d^2V/dr^2 > 0$ not satisfied at minimum
 - Numerical non-convergence

Note: The distinction between Type I/II depends on the behavior of V_{eff} near $r = 0$. In Type I, a “wall” exists near the origin requiring quantum tunneling, while in Type II, classical rolling down is possible. However, this paper does not treat dynamical evolution (tunneling rates, Friedmann equations).

2.7 Numerical Criteria

2.7.1 Search region and bound hit

Extremum search is performed over $r \in [r_{\min}, r_{\max}] = [0.01, 10^6]$. If the search result reaches near the boundary

$$r_0 < r_{\min} + \delta \quad \text{or} \quad r_0 > r_{\max} - \delta \quad (16)$$

(with $\delta = 0.02$), it is classified as bound hit and assigned Type III.

2.7.2 Barrier height ΔV definition and threshold

For Type I, barrier height ΔV is defined as:

$$\Delta V := \max_{r \in [r_{\min}, r_0]} V_{\text{eff}}(r) - V_{\text{eff}}(r_0). \quad (17)$$

Type I is determined when $\Delta V > 0$ and $dV_{\text{eff}}/dr|_{r \rightarrow 0^+} > 0$.

2.7.3 Curvature condition

The curvature at minimum r_0 is evaluated by numerical differentiation, and

$$\left. \frac{d^2 V_{\text{eff}}}{dr^2} \right|_{r=r_0} > 0 \quad (18)$$

is confirmed. If this condition is not satisfied, it is classified as Type III.

Detailed numerical parameters and edge case handling are summarized in Appendix C.

2.8 Incorporation of Nieh–Yan: FULL and Diagnostic Comparisons (TT/REE)

The primary object of this work is the **FULL** case, which incorporates the complete form of the NY density into the action. Additionally, we use **TT** and **REE** as diagnostic comparisons to disentangle the origin of FULL’s contributions.

Table 3: NY variant definitions.

Variant	NY density adopted	Purpose
FULL	$N = N_{\text{TT}} - N_{\text{REE}}$	Main result (complete NY effect)
TT	N_{TT} only	Diagnosis of torsion-torsion contribution
REE	N_{REE} only	Diagnosis of Riemann-torsion contribution

Specific processing in calculations: The engine (DPPUv2 Engine Core v3) computes N_{TT} , N_{REE} , and N_{FULL} at each step, and selects the NY density to incorporate into the Lagrangian according to the specified variant.

Significance of diagnostic comparisons: TT/REE are not proposed as independent fundamental theories but serve as auxiliary comparisons for understanding which contributions drive the phase structure of FULL. For example:

- If phase boundaries differ significantly between TT and REE \rightarrow Competition between both contributions determines phase structure
- If TT and FULL are nearly identical \rightarrow Torsion-torsion term is dominant

This diagnosis enables disentangling the geometric origin of topology dependence.

2.9 Overview of Computational Pipeline

The numerical results of this work are obtained through the computational pipeline shown in Figure 2. The pipeline consists of two major phases: the **theory building phase** (symbolic computation for deriving $V_{\text{eff}}(r)$) and the **numerical search phase** (phase classification through parameter scanning).

2.9.1 Phase 1: Theory building phase (symbolic computation)

Step 1: Geometric setup and connection calculation Set structure constants C^i_{jk} according to topology (Sec. 2.3), compute the Levi–Civita connection via the generalized Koszul formula. Derive contortion from the torsion ansatz (Sec. 2.3.3) and construct the EC connection. Automatically verify metric compatibility and Riemann tensor antisymmetry at each step.

Details of derivation are in Appendix A; engine specifications and verification are in Appendix B.

Step 2: Effective potential derivation Compute Ricci scalar R , torsion scalar $T_{abc}T^{abc}$, and NY densities (N_{TT} , N_{REE} , N_{FULL}) from the EC connection. Construct the Lagrangian density

$$\mathcal{L} = \frac{R}{2\kappa^2} + \theta_{\text{NY}}N \quad (19)$$

and obtain the effective action S_{eff} through angular integration. The effective potential is extracted as $V_{\text{eff}}(r) = -S_{\text{eff}}$.

Analytical results for each topology and NY variant are summarized in Appendix A.

2.9.2 Phase 2: Numerical search phase (parameter scan)

Step 3: Extremum search and stability determination For each parameter point $(V, \eta, \theta_{\text{NY}})$, numerically search for extrema of $V_{\text{eff}}(r)$ in the range $r \in [r_{\min}, r_{\max}]$. Use Brent's method for extremum search and verify curvature condition $d^2V_{\text{eff}}/dr^2 > 0$ by numerical differentiation.

Details of search algorithm are in Appendix C.

Step 4: Type classification and phase diagram generation Classify each parameter point as Type I/II/III according to the criteria in Sec. 2.6–2.7. Output classification results in CSV format and generate phase diagrams on the (V, η) plane.

Type determination flowchart is in Appendix C; visualization tools are in Appendix D.

2.9.3 Implementation and reproducibility

Calculations are implemented as symbolic computation using SymPy (DPPUv2 Engine Core v3), with automatic execution of consistency checks at each step (metric compatibility, three-stage verification of Riemann antisymmetry, etc.). Parameter scanning is parallelized for speed.

Engine specifications and sanity check list are in Appendix B; code and data access information are in Appendix F.

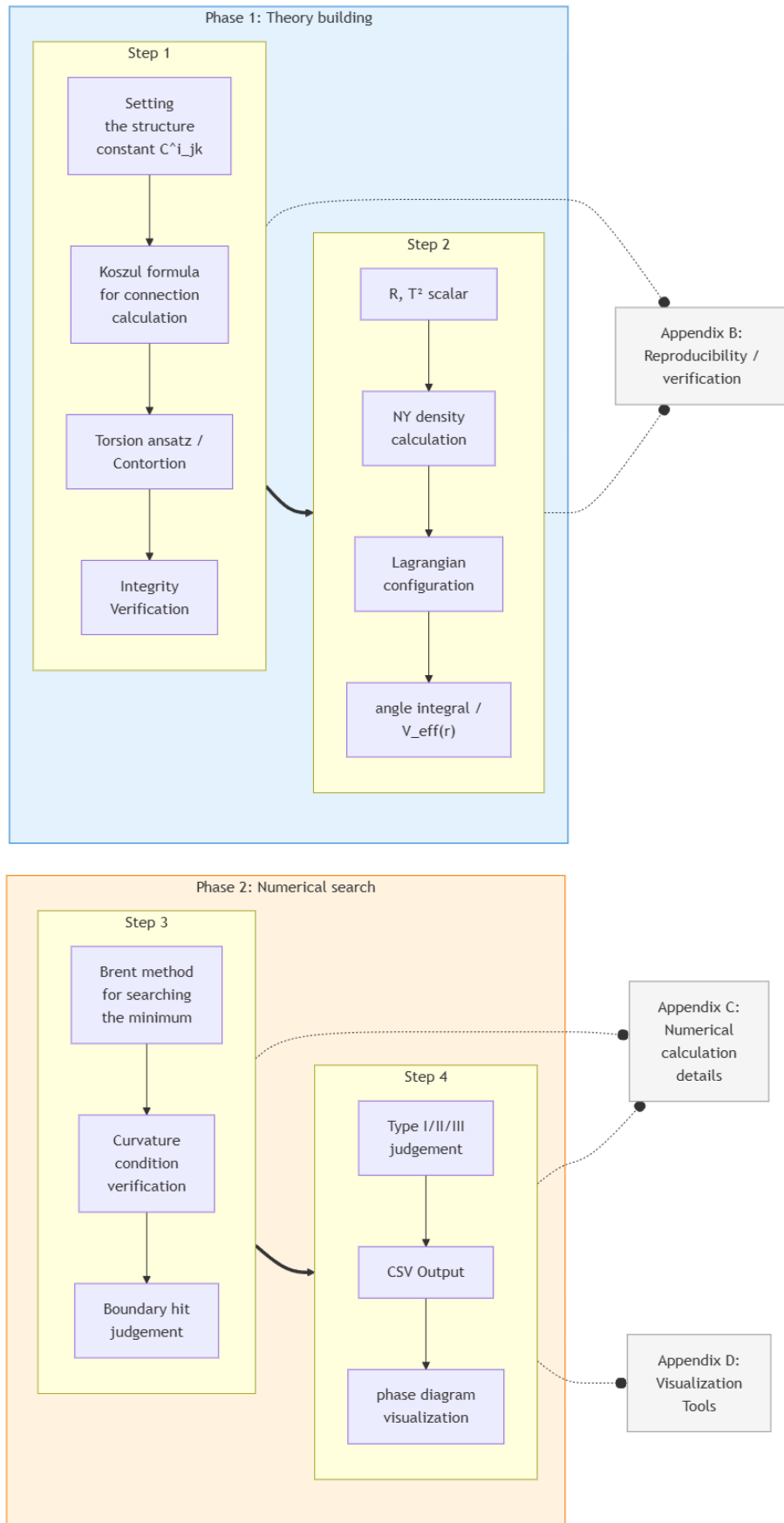


Figure 2: Computational pipeline overview.

3 Topology-Specific Reductions

This section applies the minisuperspace reduction defined in Sec. 2 to the three test beds (S^3 , T^3 , Nil^3) and derives the explicit form of the effective potential $V_{\text{eff}}(r)$ for each topology.

3.1 $S^3 \times S^1$: Reduced Action and Effective Potential

3.1.1 Geometric setup

S^3 is realized as the SU(2) group manifold, with left-invariant coframes $\{\sigma^i\}$ given by the Maurer-Cartan forms of SU(2). The structure constants are

$$C^i{}_{jk} = \frac{4}{r} \varepsilon_{ijk}, \quad (20)$$

and the background Ricci scalar (without torsion) is

$$R_{\text{LC}} = \frac{24}{r^2} > 0 \quad (21)$$

(positive curvature). The volume element is

$$\text{Vol}(S^3 \times S^1) = 2\pi^2 L r^3. \quad (22)$$

3.1.2 Scalar quantities

In MX mode ($\eta \neq 0, V \neq 0$), the scalar quantities computed by DPPUv2 Engine Core v3 are as follows:

Ricci scalar:

$$R = \frac{2(-V^2 r^2 - 9\eta^2 - 72\eta - 108)}{3r^2} \quad (23)$$

Torsion scalar:

$$T_{abc} T^{abc} = \frac{2V^2}{3} + \frac{24\eta^2}{r^2} \quad (24)$$

NY densities (each variant):

$$N_{\text{TT}} = -\frac{4V\eta}{r}, \quad N_{\text{REE}} = -\frac{2V(\eta+4)}{r}, \quad N_{\text{FULL}} = \frac{2V(4-\eta)}{r} \quad (25)$$

3.1.3 Effective potential

Integrating the Lagrangian $\mathcal{L} = R/(2\kappa^2) + \theta_{\text{NY}} N$ over the volume and extracting $V_{\text{eff}}(r) = -S_{\text{eff}}$, we obtain for each NY variant:

FULL ($N = N_{\text{FULL}}$):

$$V_{\text{eff}}^{(S^3, \text{FULL})}(r) = \frac{2\pi^2 L}{3\kappa^2} r [V^2 r^2 + 6V\kappa^2 \theta_{\text{NY}}(\eta - 4)r + 9\eta^2 + 72\eta + 108] \quad (26)$$

TT ($N = N_{\text{TT}}$):

$$V_{\text{eff}}^{(S^3, \text{TT})}(r) = \frac{2\pi^2 L}{3\kappa^2} r [V^2 r^2 + 12V\eta\kappa^2 \theta_{\text{NY}}r + 9\eta^2 + 72\eta + 108] \quad (27)$$

REE ($N = N_{\text{REE}}$):

$$V_{\text{eff}}^{(S^3, \text{REE})}(r) = \frac{2\pi^2 L}{3\kappa^2} r [V^2 r^2 + 6V\kappa^2 \theta_{\text{NY}}(\eta + 4)r + 9\eta^2 + 72\eta + 108] \quad (28)$$

These potential shapes are shown in Figure 3.

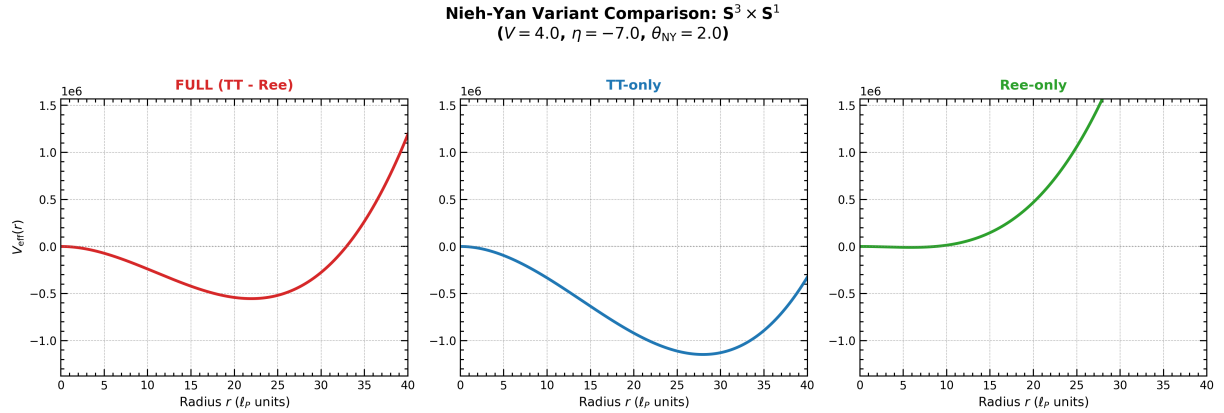


Figure 3: Nieh–Yan variant comparison for $S^3 \times S^1$.

3.1.4 Structural analysis

The effective potential for S^3 has a cubic polynomial structure in r (of the form $r^3 + r^2 + r$):

$$V_{\text{eff}}(r) \propto r \cdot [Ar^2 + Br + C], \quad (29)$$

where:

- $A = V^2 > 0$: Governs divergence as $r \rightarrow \infty$ (always positive)
- B : Proportional to NY coupling θ_{NY} , depends on η (sign can vary)
- $C = 9\eta^2 + 72\eta + 108 = 9(\eta + 4)^2 - 36$: Takes minimum value -36 at $\eta = -4$

From this structure, a local minimum can appear when $B < 0$ and $|B|$ is sufficiently large. In particular, for the FULL variant, $B \propto (\eta - 4)$, so $B < 0$ for $\eta < 4$, meaning local minima can appear even in the $\eta > 0$ region.

The contributions of r^3 , r^2 , and r terms to the potential are shown in Figure 4.

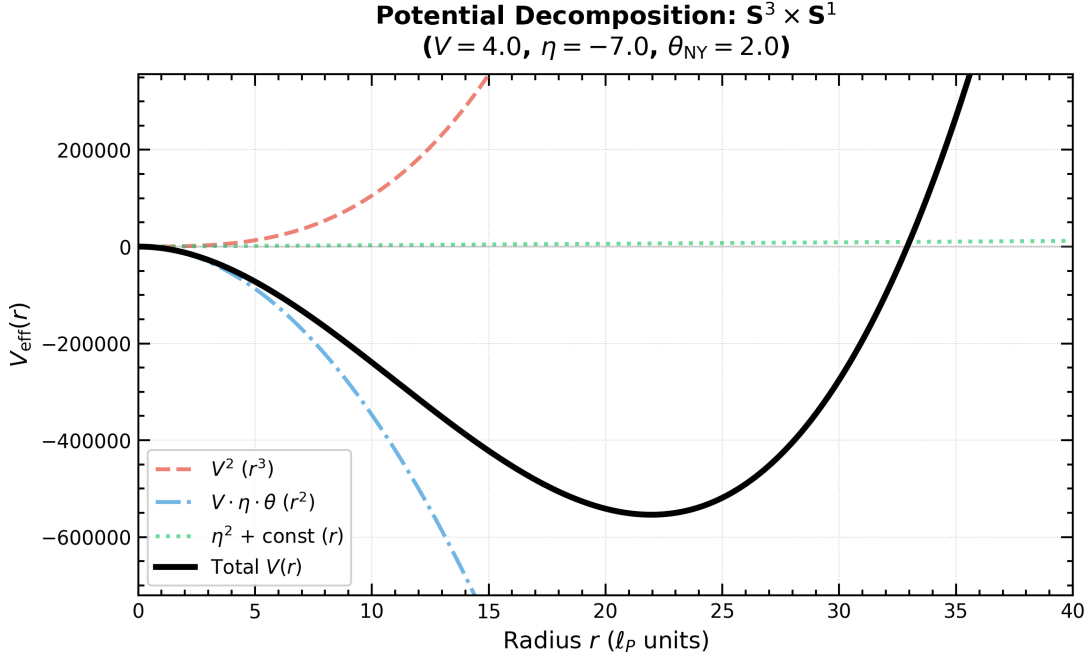


Figure 4: Potential decomposition for $S^3 \times S^1$.

3.2 $T^3 \times S^1$: Reduced Action and Effective Potential

3.2.1 Geometric setup

T^3 is an Abelian group (discrete quotient of \mathbb{R}^3), with all structure constants vanishing:

$$C^i{}_{jk} = 0. \quad (30)$$

The background Ricci scalar is

$$R_{\text{LC}} = 0 \quad (31)$$

(flat). The volume element is

$$\text{Vol}(T^3 \times S^1) = (2\pi)^4 L R_1 R_2 R_3, \quad (32)$$

where R_1, R_2, R_3 are the circumferences in each direction of T^3 . In this paper, for comparison with S^3 and Nil^3 , we assume isotropic expansion $R_1 = R_2 = R_3 = r$. This allows description with a single scale parameter r , as with the other topologies.

3.2.2 Scalar quantities

In MX mode, the scalar quantities are:

Ricci scalar:

$$R = -\frac{2V^2}{3} - \frac{6\eta^2}{r^2} \quad (33)$$

Torsion scalar:

$$T_{abc}T^{abc} = \frac{2V^2}{3} + \frac{24\eta^2}{r^2} \quad (34)$$

NY densities (each variant):

$$N_{\text{TT}} = -\frac{4V\eta}{r}, \quad N_{\text{REE}} = -\frac{2V\eta}{r}, \quad N_{\text{FULL}} = -\frac{2V\eta}{r} \quad (35)$$

Notably, for T^3 , $N_{\text{FULL}} = N_{\text{REE}}$. This is due to the zero background curvature.

3.2.3 Effective potential

With the isotropic setting $R_1 = R_2 = R_3 = r$, for each NY variant:

FULL (= REE):

$$V_{\text{eff}}^{(T^3, \text{FULL})}(r) = \frac{16\pi^4 L}{3\kappa^2} [V^2 r^3 + 6V\eta\kappa^2\theta_{\text{NY}}r^2 + 9\eta^2 r] \quad (36)$$

TT:

$$V_{\text{eff}}^{(T^3, \text{TT})}(r) = \frac{16\pi^4 L}{3\kappa^2} [V^2 r^3 + 12V\eta\kappa^2\theta_{\text{NY}}r^2 + 9\eta^2 r] \quad (37)$$

These have the same $r^3 + r^2 + r$ structure as S^3 .

The potential shapes are shown in Figure 5.

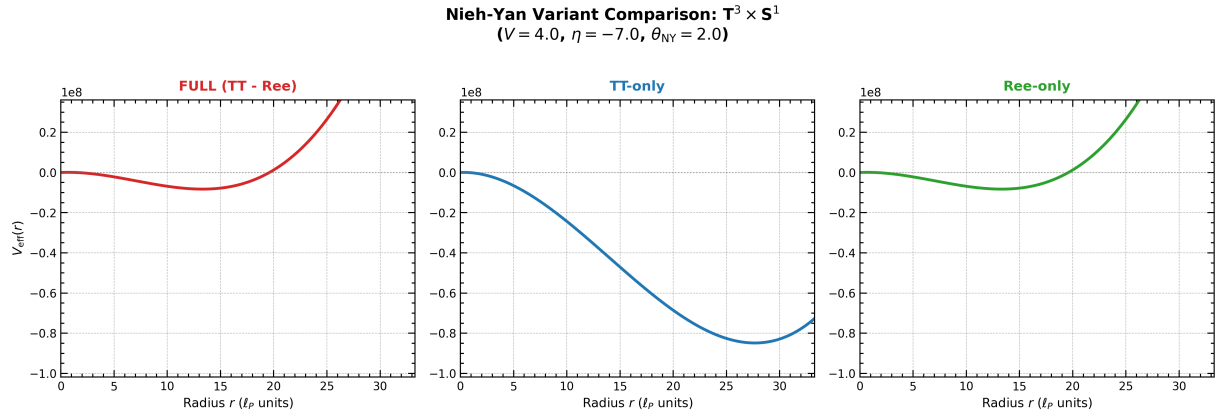


Figure 5: Nieh–Yan variant comparison for $T^3 \times S^1$.

3.2.4 Structural analysis

With the isotropic setting, the effective potential for T^3 has the same structure as S^3 and Nil^3 :

$$V_{\text{eff}}(r) \propto r \cdot [V^2 r^2 + Br + C], \quad (38)$$

where $B = 6V\eta\kappa^2\theta_{\text{NY}}$ and $C = 9\eta^2$.

From this form:

- $r \rightarrow 0$: $V_{\text{eff}} \rightarrow 0^+$ (always positive for $C > 0$ when $\eta \neq 0$)
- $r \rightarrow \infty$: $V_{\text{eff}} \rightarrow +\infty$ due to the r^3 term
- Minimum existence condition: $3V^2r^2 + 2Br + C = 0$ has positive real solutions

A characteristic of T^3 is that the coefficient $C = 9\eta^2$ of r is always non-negative (zero only when $\eta = 0$). Therefore:

- For $\theta_{\text{NY}} = 0$, $B = 0$, and $dV_{\text{eff}}/dr \propto 3V^2r^2 + 9\eta^2 > 0$ (for $r > 0$), so it is always monotonically increasing (Type III)
- For $\theta_{\text{NY}} > 0$ and $\eta < 0$, $B < 0$, and minima can form

Under $\eta \rightarrow -\eta$ transformation, $B \rightarrow -B$, so for $\theta_{\text{NY}} \neq 0$, symmetry is broken. For $\theta_{\text{NY}} > 0$, stable regions appear only on the $\eta < 0$ side.

The contributions of r^3 , r^2 , and r terms are shown in Figure 6.

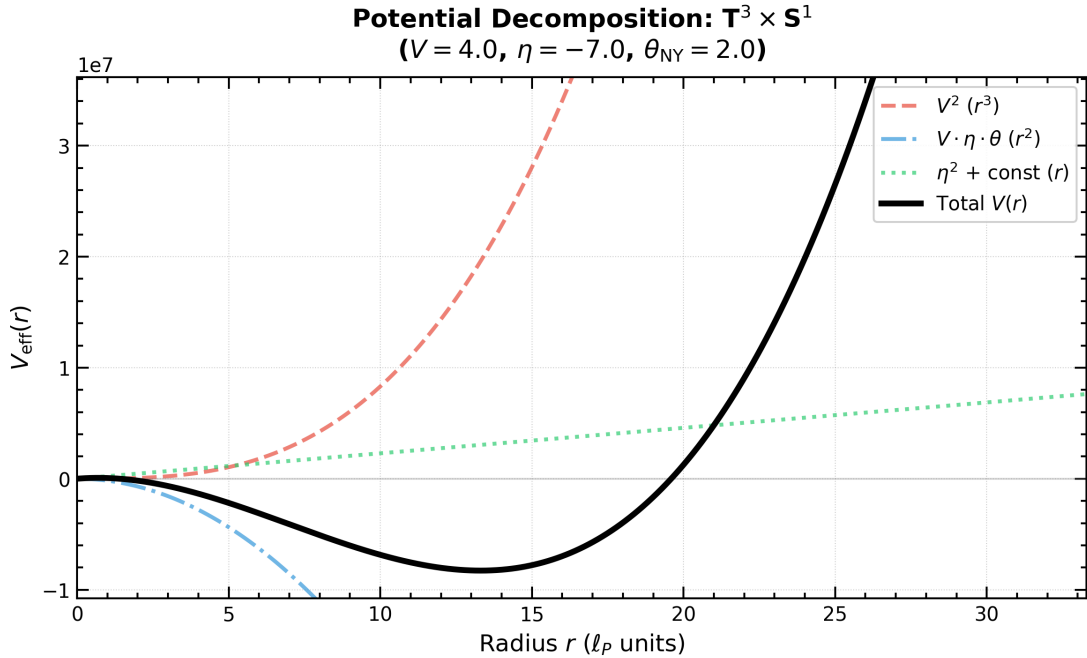


Figure 6: Potential decomposition for $T^3 \times S^1$.

3.3 $\text{Nil}^3 \times S^1$: Reduced Action and Effective Potential

3.3.1 Geometric setup

Nil^3 is a compact quotient of the Heisenberg group (Bianchi Type II), with structure constants

$$C^2_{01} = -\frac{1}{r}, \quad C^2_{10} = +\frac{1}{r}, \quad \text{others } 0. \quad (39)$$

An important point is that Nil^3 is **not bi-invariant** (the Heisenberg group is nilpotent, not semisimple). Therefore, the generalized Koszul formula (see Appendix A) must be used for connection calculations.

The background Ricci scalar is

$$R_{\text{LC}} = -\frac{1}{2r^2} < 0 \quad (40)$$

(negative curvature). The volume element is

$$\text{Vol}(\text{Nil}^3 \times S^1) = (2\pi)^4 L r^3. \quad (41)$$

3.3.2 Scalar quantities

In MX mode, the scalar quantities are:

Ricci scalar:

$$R = \frac{-4V^2 r^2 - 36\eta^2 + 24\eta + 9}{6r^2} \quad (42)$$

Torsion scalar:

$$T_{abc} T^{abc} = \frac{2V^2}{3} + \frac{24\eta^2}{r^2} \quad (43)$$

NY densities (each variant):

$$N_{\text{TT}} = -\frac{4V\eta}{r}, \quad N_{\text{REE}} = \frac{2V(1-3\eta)}{3r}, \quad N_{\text{FULL}} = -\frac{2V(3\eta+1)}{3r} \quad (44)$$

3.3.3 Effective potential

For each NY variant:

FULL:

$$V_{\text{eff}}^{(\text{Nil}^3, \text{FULL})}(r) = \frac{4\pi^4 L}{3\kappa^2} r [4V^2 r^2 + 8V\kappa^2 \theta_{\text{NY}}(3\eta+1)r + 36\eta^2 - 24\eta - 9] \quad (45)$$

TT:

$$V_{\text{eff}}^{(\text{Nil}^3, \text{TT})}(r) = \frac{4\pi^4 L}{3\kappa^2} r [4V^2 r^2 + 48V\eta\kappa^2 \theta_{\text{NY}} r + 36\eta^2 - 24\eta - 9] \quad (46)$$

REE:

$$V_{\text{eff}}^{(\text{Nil}^3, \text{REE})}(r) = \frac{4\pi^4 L}{3\kappa^2} r [4V^2 r^2 + 8V\kappa^2 \theta_{\text{NY}}(3\eta-1)r + 36\eta^2 - 24\eta - 9] \quad (47)$$

The potential shapes are shown in Figure 7.

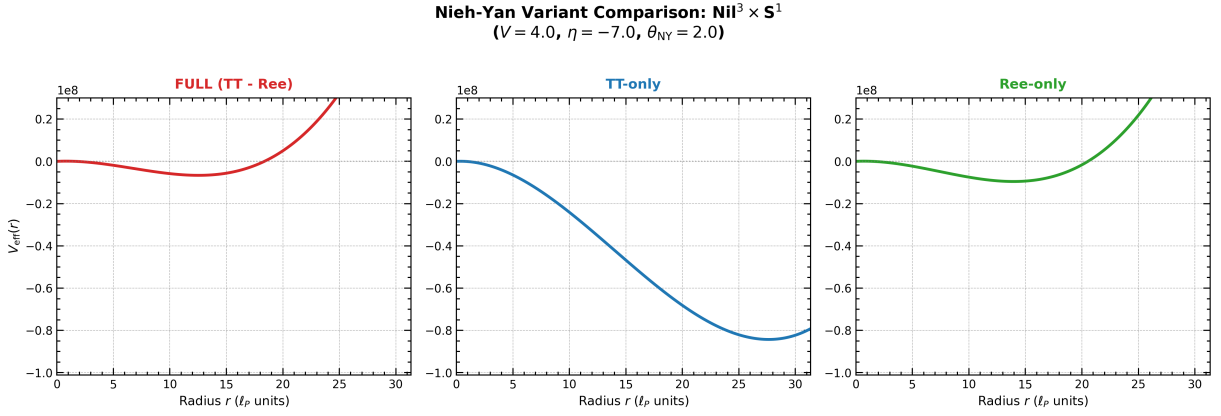


Figure 7: Nieh–Yan variant comparison for $\text{Nil}^3 \times S^1$.

3.3.4 Structural analysis

The effective potential for Nil^3 also has the $r^3 + r^2 + r$ structure like S^3 , but the sign of coefficients brings differences:

$$C_{\text{Nil}^3} = 36\eta^2 - 24\eta - 9 = 36 \left(\eta - \frac{1}{3} \right)^2 - 13. \quad (48)$$

This quadratic function takes minimum value -13 at $\eta = 1/3$, and becomes negative in the range $\eta \in (-0.27, 0.94)$.

When the coefficient C of r is negative, $V_{\text{eff}}(r) \rightarrow 0^-$ as $r \rightarrow 0$, meaning the potential takes negative values near the origin. This contrasts with S^3 (where $C > 0$ over a wide region), suggesting that for Nil^3 with small θ_{NY} values, the stable region is limited to a narrow band.

The contributions of r^3 , r^2 , and r terms are shown in Figure 8.

3.4 Structural Comparison: Sources of Topology Dependence

We compare the structure of effective potentials across the three topologies and organize the sources of topology dependence.

3.4.1 General form of effective potential

For all topologies, the effective potential in MX mode is expressed in the general form:

$$V_{\text{eff}}(r) = \mathcal{N} \cdot r^\alpha \cdot P(r), \quad (49)$$

where \mathcal{N} is a normalization factor, α is a topology-dependent exponent, and $P(r)$ is a polynomial in r .

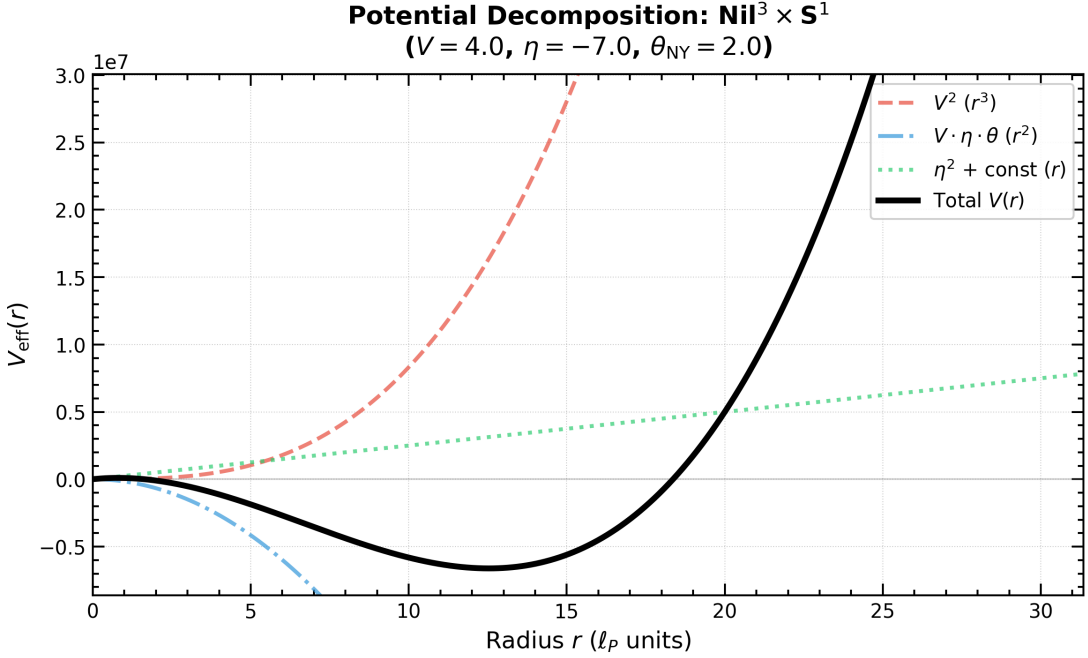


Figure 8: Potential decomposition for $\text{Nil}^3 \times S^1$.

Table 4: Effective potential structure comparison.

Topology	Structure	$r \rightarrow 0$	$r \rightarrow \infty$
S^3	$r \cdot [Ar^2 + Br + C]$	$\rightarrow 0$	$\rightarrow +\infty$
T^3	$r \cdot [Ar^2 + Br + C]$	$\rightarrow 0$	$\rightarrow +\infty$
Nil^3	$r \cdot [Ar^2 + Br + C]$	$\rightarrow 0$	$\rightarrow +\infty$

All of S^3 , T^3 , and Nil^3 share the $r \cdot [Ar^2 + Br + C]$ structure.

3.4.2 Comparison of NY densities

Table 5: Comparison of NY densities (N_{FULL}) and background curvature dependence.

Topology	N_{FULL}	Background curvature dependence
S^3	$\frac{2V(4-\eta)}{r}$	$(4-\eta)$: contribution from positive curvature
T^3	$-\frac{2V\eta}{r}$	η only: no curvature contribution
Nil^3	$-\frac{2V(3\eta+1)}{3r}$	$(3\eta+1)$: contribution from negative curvature

The factor $(4 - \eta)$ appearing in N_{FULL} for S^3 originates from the $(\eta + 4)$ term in N_{REE} . This $+4$ reflects coupling with the positive background curvature ($R_{\text{LC}} = 24/r^2$).

In contrast, for T^3 , the background curvature is zero, so there is no curvature contribution to N_{FULL} .

3.4.3 Geometric factors affecting stability

The existence and position of the effective potential minimum are primarily determined by the following factors:

1. **Coefficient of r^3 term ($\propto V^2$)**: Always positive. Governs growth as $r \rightarrow \infty$.
2. **Coefficient of r^2 term ($\propto V\theta_{\text{NY}} \times f(\eta)$)**: Function of NY coupling and η . When negative, promotes minimum formation.
3. **Coefficient of r term**: Topology-specific geometric contribution.
 - S^3 : $9(\eta + 4)^2 - 36$
 - T^3 : $9\eta^2$
 - Nil^3 : $36(\eta - 1/3)^2 - 13$

The competition among these factors produces different phase structures for each topology. Detailed analysis of phase boundaries is presented in Sec. 4.

4 Numerical Results: Phase Diagrams and Boundaries

This section presents the results of numerical scanning on the effective potentials derived in Sec. 3. We first explain the Type classification procedure and how to read phase diagrams, then show the phase diagrams for each topology. The mechanisms of phase boundary formation and geometric interpretation are discussed in Sec. 5.

4.1 Type Classification Procedure

4.1.1 Search region and numerical method

For each parameter point $(V, \eta, \theta_{\text{NY}})$, we numerically search for extrema of $V_{\text{eff}}(r)$ in the range $r \in [r_{\min}, r_{\max}] = [0.01, 10^6]$. We use Brent's method (`scipy.optimize.minimize_scalar`) for extremum search and verify the curvature condition $d^2V/dr^2 > 0$ by numerical differentiation.

4.1.2 Type determination criteria

Based on the definitions in Sec. 2.6, we determine Types using the following criteria:

- **Type I (stable with barrier):** A local minimum r_0 exists within the allowed region, and a barrier ($\Delta V > 0$) exists in the $r \rightarrow 0$ direction
- **Type II (rolling):** A local minimum r_0 exists within the allowed region, but no barrier in the $r \rightarrow 0$ direction ($dV_{\text{eff}}/dr|_{r \rightarrow 0^+} < 0$)
- **Type III (unstable):** No stable local minimum exists within the allowed region, or search reaches boundary (r_{\min} or r_{\max})

4.1.3 Scan resolution

The scan resolution is 51 points in the V direction, 151 points in the η direction, and 51 points in the θ_{NY} direction (range $[0, 5]$), giving approximately 390,000 evaluations per topology. Note that this paper primarily presents results for $\theta_{\text{NY}} \lesssim 2$. The uncertainty in boundary positions is on the order of the grid spacing ($\Delta\eta \approx 0.1$, $\Delta V \approx 0.1$).

4.2 How to Read Phase Diagrams

In the phase diagrams of this paper, Type classification is displayed on the (V, η) plane using the following visual conventions:

- **Colored region (no hatching):** Type I (metastable well with barrier)

- **Colored region (with hatching):** Type II (rolling, no barrier)
- **White region:** Type III (unstable / boundary-attached)

The color gradient represents the logarithmic value of the stable radius $\log_{10}(r_0)$, ranging from purple (small) to yellow (large). White contour lines show the logarithmic barrier height/well depth $\log_{10}(\Delta V)$.

4.3 Phase Diagrams by Topology: FULL Variant

4.3.1 $S^3 \times S^1$

Figure 9 shows the phase diagrams for S^3 -FULL at $\theta_{\text{NY}} = 0, 1, 2$.

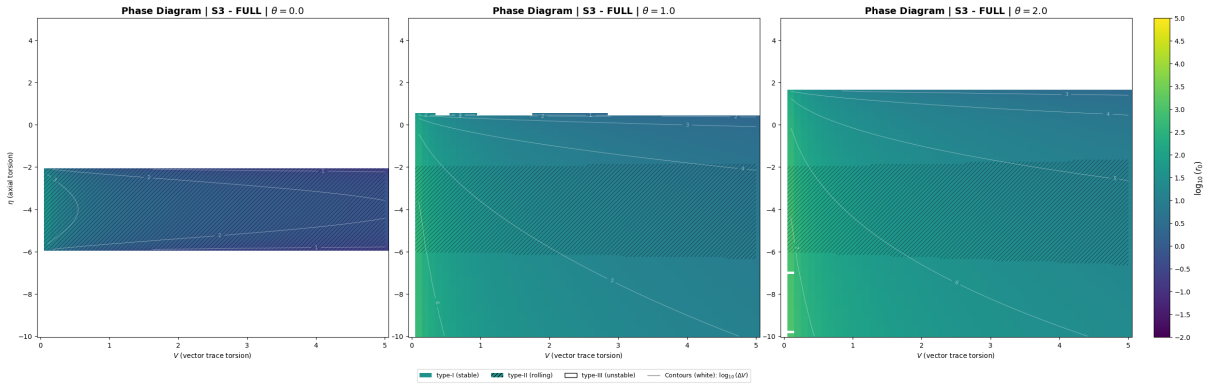


Figure 9: Phase diagram: $S^3 \times S^1$ ($\theta_{\text{NY}} = 0, 1, 2$).

For $\theta_{\text{NY}} = 0$:

- $\eta \gtrsim -2$: Type III (white) dominates
- $-6 \lesssim \eta \lesssim -2$: Band-like region of Type II (hatched)
- $\eta \lesssim -6$: Type III again

For $\theta_{\text{NY}} = 1$:

- $\eta \gtrsim 0.5$: Type III (white)
- $-2 \lesssim \eta \lesssim 0.5$: Type I (no hatching)
- $-6 \lesssim \eta \lesssim -2$: Band-like region of Type II (hatched)
- $\eta \lesssim -6$: Type I (no hatching) reappears

For $\theta_{\text{NY}} = 2$:

- Stable region (Type I + II) expands toward $\eta > 0$
- I/III boundary moves to around $\eta \approx 2$
- Type II band also expands

Key observations:

1. $\theta_{\text{NY}} = 0$: Only main band of Type II
2. $\theta_{\text{NY}} > 0$: Type I region appears and expands
3. $\eta \rightarrow -\eta$ symmetry is broken

4.3.2 $T^3 \times S^1$

Figure 10 shows the phase diagrams for T^3 -FULL at $\theta_{\text{NY}} = 0, 1, 2$.

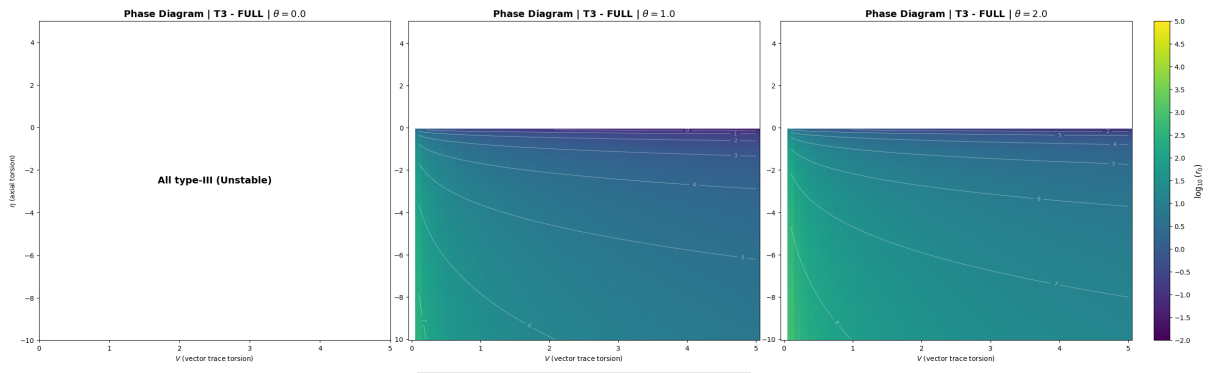


Figure 10: Phase diagram: $T^3 \times S^1$ ($\theta_{\text{NY}} = 0, 1, 2$).

For $\theta_{\text{NY}} = 0$:

- Entire region is Type III (monotonically increasing)
- No stable minimum exists

For $\theta_{\text{NY}} = 1$:

- Type I (stable well) appears in wide region of $\eta < 0$
- $\eta \gtrsim 0$ is entirely Type III

For $\theta_{\text{NY}} = 2$:

- Type I region expands further
- Contour lines of r_0 extend in negative η direction

Key observations:

1. $\theta_{\text{NY}} = 0$: Entire region Type III
2. $\theta_{\text{NY}} > 0$: Type I appears
3. $\eta \rightarrow -\eta$ symmetry is broken

4.3.3 $\text{Nil}^3 \times S^1$

Figure 11 shows the phase diagrams for Nil^3 -FULL at $\theta_{\text{NY}} = 0, 1, 2$.

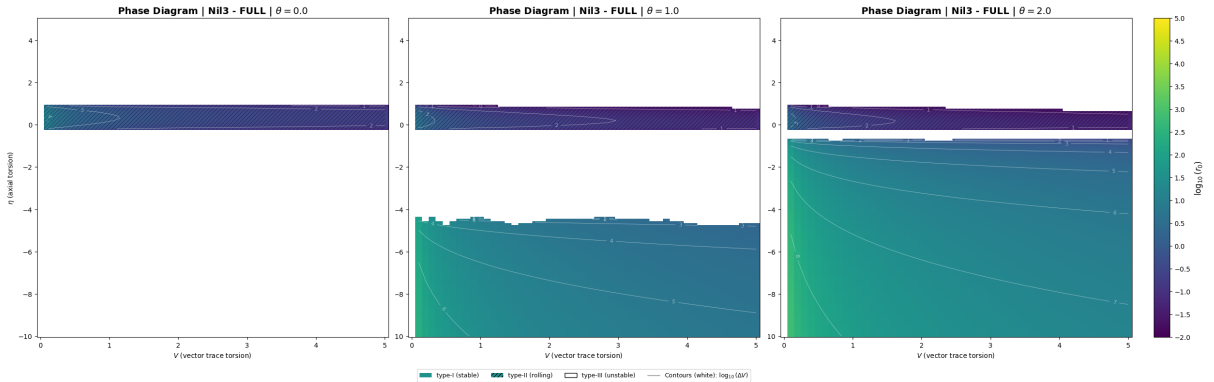


Figure 11: Phase diagram: $\text{Nil}^3 \times S^1$ ($\theta_{\text{NY}} = 0, 1, 2$).

For $\theta_{\text{NY}} = 0$:

- $-0.3 \lesssim \eta \lesssim 1$: Narrow stable band (Type II)
- $\eta < -0.3$ and $\eta > 1$: Type III (white) dominates almost the entire region

For $\theta_{\text{NY}} = 1$:

- Main band ($-0.3 < \eta < 1$) is maintained
- **Separate stable region (Type I)** appears at $\eta \lesssim -4$
- Main band and separate stable region are separated by Type III region

For $\theta_{\text{NY}} = 2$:

- Lower stable region expands, distributing widely at $\eta \lesssim -0.5$
- Width of main band ($-0.3 < \eta < 1$) gradually decreases in large V region

Key observations:

1. $\theta_{\text{NY}} = 0$: Only main band of Type II
2. $\theta_{\text{NY}} > 0$: Type I region appears and expands
3. $\eta \rightarrow -\eta$ symmetry is broken

4.4 Summary of θ_{NY} Dependence

Tables 6–8 summarize the θ_{NY} dependence of phase boundaries for each topology.

Table 6: S^3 : θ_{NY} dependence of phase boundary positions (FULL variant).

Type	$\theta_{\text{NY}} = 0$	$\theta_{\text{NY}} = 1$	$\theta_{\text{NY}} = 2$
Type I region	None	$\eta < -6, -2 < \eta < 0.5$	Expanded
Type II (main band)	$-6 \lesssim \eta \lesssim -2$	$-6 \lesssim \eta \lesssim -2$	$-6 \lesssim \eta \lesssim -2$
Type III region	$\eta \lesssim -6, -2 \lesssim \eta$	$0.5 \lesssim \eta$	Shrunk

Table 7: T^3 : θ_{NY} dependence of phase boundary positions (FULL variant).

Type	$\theta_{\text{NY}} = 0$	$\theta_{\text{NY}} = 1$	$\theta_{\text{NY}} = 2$
Type I region	None	$\eta \lesssim 0$	$\eta \lesssim 0$
Type II region	None	None	None
Type III region	Entire	$0 \lesssim \eta$	$0 \lesssim \eta$

Table 8: Nil^3 : θ_{NY} dependence of phase boundary positions (FULL variant).

Type	$\theta_{\text{NY}} = 0$	$\theta_{\text{NY}} = 1$	$\theta_{\text{NY}} = 2$
Type I region	None	$\eta \lesssim -4$	$\eta < -0.5$
Type II (main band)	$-0.3 \lesssim \eta \lesssim 1$	$-0.3 \lesssim \eta \lesssim 1$	$-0.3 \lesssim \eta \lesssim 1$
Type III region	$\eta \lesssim -0.3, 1 \lesssim \eta$	$-4 \lesssim \eta \lesssim -0.3, 1 \lesssim \eta$	$-0.5 \lesssim \eta \lesssim -0.3, 1 \lesssim \eta$

Key observations:

1. S^3 : Shows strong dependence on θ_{NY} , with stable region expanding toward $\eta > 0$
2. T^3 : Entire region is Type III for $\theta_{\text{NY}} \lesssim 0.9$, but Type I appears in $\eta < 0$ for $\theta_{\text{NY}} \gtrsim 0.9$
3. Nil^3 : Main band is insensitive to θ_{NY} , but stable region in $\eta < 0$ grows with θ_{NY}

4.5 Comparison with TT/REE Variants

Figure 12 shows the phase diagram matrix for 3 topologies \times 3 variants at $\theta_{\text{NY}} = 1.0$.

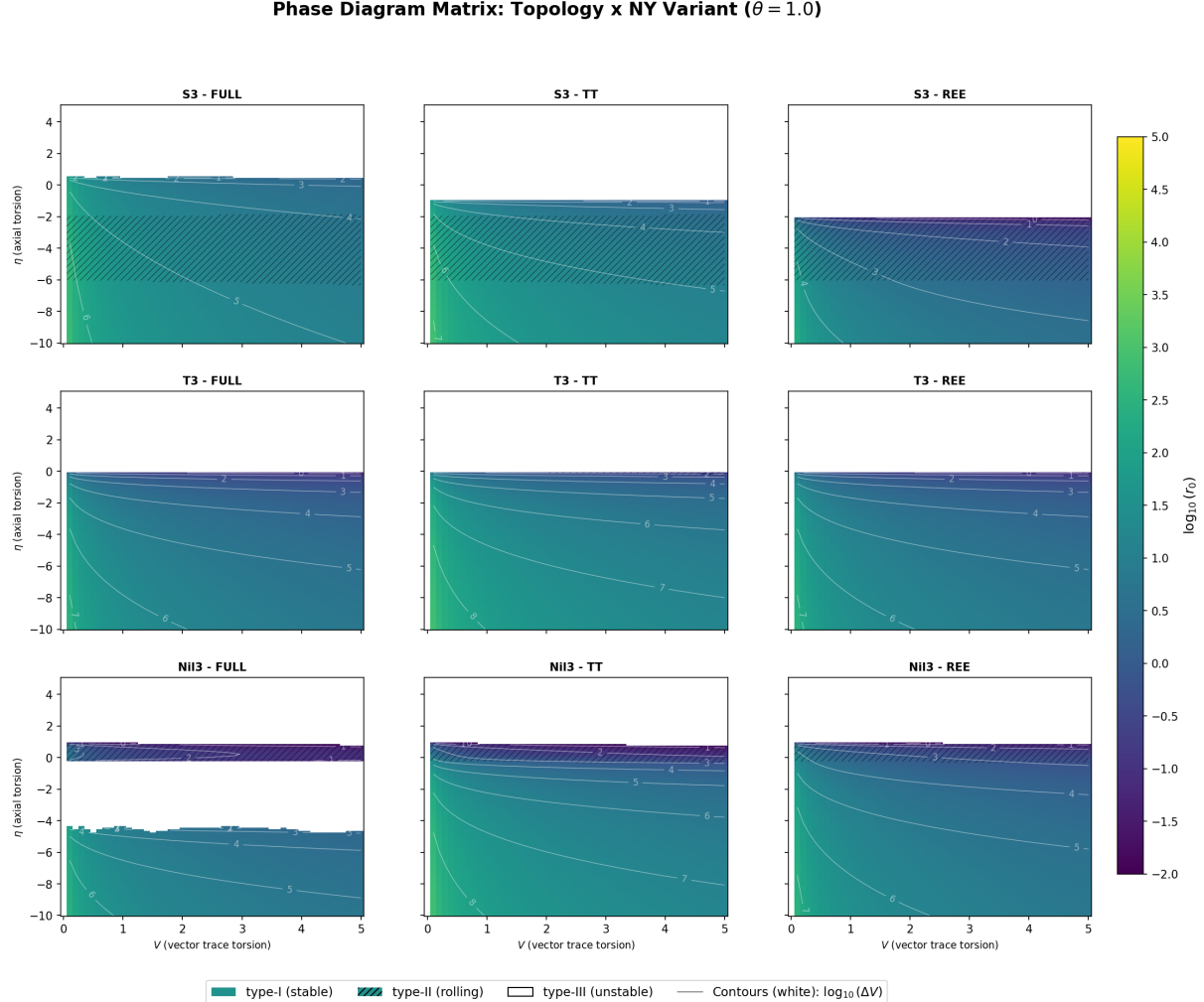


Figure 12: Phase diagram matrix: $\theta_{\text{NY}} = 1.0$.

S^3 :

- Phase boundary positions clearly differ among FULL, TT, REE
- FULL has the widest stable region
- TT and REE have narrower stable regions than FULL

T^3 :

- FULL and REE have completely identical phase diagrams (because $N_{\text{FULL}} = N_{\text{REE}}$)
- TT differs by a factor of 2 in coefficient, but phase boundary positions are similar
- For $\theta_{\text{NY}} \gtrsim 0.9$, Type I region appears in $\eta < 0$ for all variants

NiI³:

- Moderate differences observed among the 3 variants
- Main band positions are nearly identical
- Shape and extent of lower stable region differ

5 Mechanisms and Interpretation of Phase Structure

This section interprets the features of the phase diagrams presented in Sec. 4 based on the analytical structure of the effective potential $V_{\text{eff}}(r)$.

5.1 Shape Changes of $V_{\text{eff}}(r)$ at Type Transitions

5.1.1 Type III \rightarrow Type II transition (appearance of well)

The transition from Type III to Type II corresponds to the appearance of a local minimum in $V_{\text{eff}}(r)$.

Consider the case of S^3 -FULL with $\theta_{\text{NY}} = 0$, $V = 2$ fixed, and η varying from 0 to -2 :

- $\eta = 0$ (**Type III**): $V_{\text{eff}}(r)$ is monotonically increasing with no minimum within the allowed region
- $\eta = -2$ (**Type II**): A local minimum appears in $V_{\text{eff}}(r)$. However, there is no barrier in the $r \rightarrow 0$ direction, with $dV_{\text{eff}}/dr < 0$ near the origin

This transition can be understood from the effective potential structure derived in Sec. 3. For S^3 :

$$V_{\text{eff}}(r) \propto r [V^2 r^2 + Br + C], \quad (50)$$

where $B = 6V\kappa^2\theta_{\text{NY}}(\eta - 4)$ and $C = 9\eta^2 + 72\eta + 108 = 9(\eta + 4)^2 - 36$.

For $\theta_{\text{NY}} = 0$, $B = 0$, and minimum existence is determined solely by the sign of C . Minima can appear in the range $\eta \in (-8, 0)$ where $C < 0$, but due to the behavior as $r \rightarrow 0$, this results in Type II.

5.1.2 Type II \rightarrow Type I transition (barrier formation)

The transition from Type II to Type I corresponds to barrier formation in the $r \rightarrow 0$ direction.

This transition is characterized by a sign change of the gradient of $V_{\text{eff}}(r)$ near the origin:

$$\left. \frac{dV_{\text{eff}}}{dr} \right|_{r \rightarrow 0^+} \begin{cases} < 0 & (\text{Type II: rolling}) \\ > 0 & (\text{Type I: barrier}) \end{cases} \quad (51)$$

Differentiating the effective potential for S^3 :

$$\frac{dV_{\text{eff}}}{dr} \propto 3V^2 r^2 + 2Br + C. \quad (52)$$

As $r \rightarrow 0$, $dV_{\text{eff}}/dr \propto C$, so **the sign of C determines Type I/II**:

- $C > 0$: $dV_{\text{eff}}/dr|_{r=0} > 0 \rightarrow$ Type I

- $C < 0$: $dV_{\text{eff}}/dr|_{r=0} < 0 \rightarrow \text{Type II}$

For S^3 , $C = 9(\eta + 4)^2 - 36$, and $C = 0$ at $\eta = -4 \pm 2$, i.e., $\eta = -2$ or $\eta = -6$. These correspond to the I/II boundary positions.

5.1.3 Type I \rightarrow Type II \rightarrow Type I re-transition

The “Type I \rightarrow Type II \rightarrow Type I” re-transition observed for S^3 -FULL with $\theta_{\text{NY}} \geq 1$ can be understood from the fact that $C(\eta) = 9(\eta + 4)^2 - 36$ is a quadratic function.

$C(\eta)$ takes minimum value -36 at $\eta = -4$, and $C = 0$ at $\eta = -2$ and $\eta = -6$. Therefore:

- $\eta > -2$: $C > 0 \rightarrow \text{Type I (or Type III)}$
- $-6 < \eta < -2$: $C < 0 \rightarrow \text{Type II}$
- $\eta < -6$: $C > 0 \rightarrow \text{Type I}$

This structure produces the Type I \rightarrow Type II \rightarrow Type I re-transition as η varies from positive to negative.

5.2 Origin of Complex Phase Structure in S^3

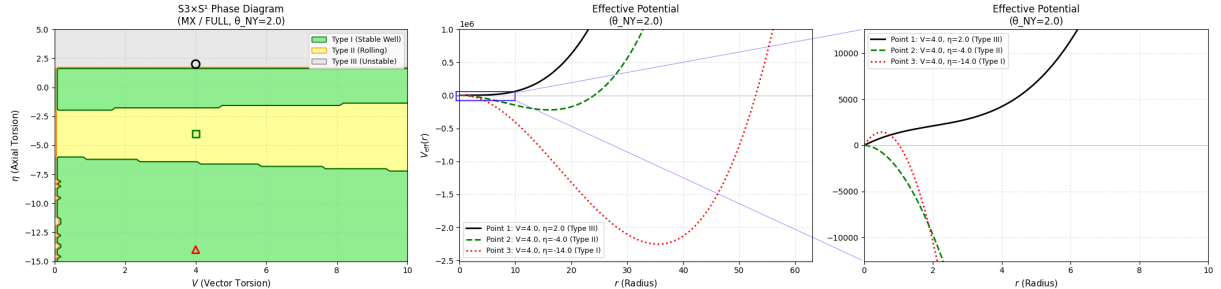


Figure 13: Phase-potential correspondence for $S^3 \times S^1$ ($\theta_{\text{NY}} = 2$).

Observed features:

1. For $\theta_{\text{NY}} = 0$, only a band-like Type II region exists, with no Type I
2. For $\theta_{\text{NY}} > 0$, as shown in Figure 13, Type I bands appear and expand with increasing θ_{NY}
3. A “re-transition” structure of Type I \rightarrow Type II \rightarrow Type I is observed for $\theta_{\text{NY}} \geq 1$
4. Stable radius r_0 tends to increase as η becomes more negative
5. $\eta \rightarrow -\eta$ symmetry is broken

The reason S^3 exhibits complex phase structure is due to competition between two factors:

5.2.1 Role of coefficient B (θ_{NY} dependence)

The coefficient of the r^2 term, $B = 6V\kappa^2\theta_{\text{NY}}(\eta - 4)$, has the following effects for $\theta_{\text{NY}} > 0$:

- For $\eta < 4$, $B < 0$: Adds negative contribution to $V_{\text{eff}}(r)$, promoting minimum formation
- $|B|$ increases proportionally with θ_{NY}

For $\theta_{\text{NY}} = 0$, $B = 0$, and minimum existence is determined by C alone. When $\theta_{\text{NY}} > 0$, the contribution of B is added, and minima can form even in regions where $C > 0$. This is the mechanism for “expansion of stable region with increasing θ_{NY} ”.

5.2.2 Role of coefficient C (Type I/II boundary)

The coefficient of r , $C = 9(\eta + 4)^2 - 36$, governs the behavior as $r \rightarrow 0$ and determines Type I/II.

Importantly, the factor $(\eta + 4)$ appearing in the expression for C reflects coupling with the positive background curvature $R_{\text{LC}} = 24/r^2$ of S^3 . As seen in Sec. 3, $(\eta + 4)$ appears in $N_{\text{REE}} = -2V(\eta + 4)/r$, which propagates to C .

5.2.3 Origin of the factor $(\eta - 4)$

The factor $B \propto (\eta - 4)$ in the FULL variant is directly derived from $N_{\text{FULL}} = N_{\text{TT}} - N_{\text{REE}} = 2V(4 - \eta)/r$.

This factor differs from both TT ($B \propto \eta$) and REE ($B \propto \eta + 4$), being unique to FULL. Due to $(\eta - 4)$, $B < 0$ over the wide range $\eta < 4$, which is the reason FULL has stable regions even for $\eta > 0$.

5.3 Phase Structure of T^3 : θ_{NY} Threshold and η Asymmetry

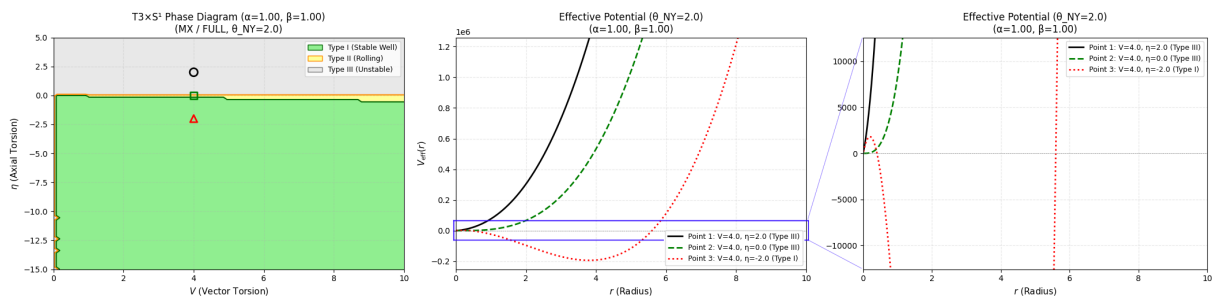


Figure 14: Phase-potential correspondence for $T^3 \times S^1$ ($\theta_{\text{NY}} = 2$).

Observed features:

- $\theta_{\text{NY}} \lesssim 0.9$: Entire region is Type III
- $\theta_{\text{NY}} \gtrsim 0.9$: As shown in Figure 14, Type I appears in $\eta < 0$
- $\eta \rightarrow -\eta$ symmetry is broken (prominent for $\theta_{\text{NY}} > 0$)

We analyze the phase structure of T^3 with the isotropic setting $R_1 = R_2 = R_3 = r$.

5.3.1 Effective potential structure

The effective potential for T^3 is:

$$V_{\text{eff}}(r) \propto r \cdot [V^2 r^2 + Br + C], \quad (53)$$

where $B = 6V\eta\kappa^2\theta_{\text{NY}}$ and $C = 9\eta^2$. This has the same $r^3 + r^2 + r$ structure as S^3 .

5.3.2 Entire Type III for $\theta_{\text{NY}} = 0$

For $\theta_{\text{NY}} = 0$, $B = 0$, giving:

$$V_{\text{eff}}(r) \propto r(V^2 r^2 + 9\eta^2). \quad (54)$$

Since $C = 9\eta^2 \geq 0$ and $V^2 > 0$, the bracketed term is always positive, and $V_{\text{eff}}(r)$ is monotonically increasing for $r > 0$. Therefore, the entire parameter region is Type III (unstable).

This originates from the flatness of T^3 ($R_{\text{LC}} = 0$): since there is no contribution from background curvature, the coefficient C of r contains no first-order term in η , and $C = 9\eta^2$ is always non-negative.

5.3.3 Type I appearance for $\theta_{\text{NY}} > 0$

For $\theta_{\text{NY}} > 0$, $B = 6V\eta\kappa^2\theta_{\text{NY}}$ becomes effective.

The condition for minimum existence is that $dV_{\text{eff}}/dr = 0$ has positive solutions:

$$3V^2 r^2 + 2Br + C = 0. \quad (55)$$

The discriminant $D = 4B^2 - 12V^2C = 4(B^2 - 3V^2C)$ must be positive, and the solutions must be positive:

$$B < 0 \quad \text{and} \quad B^2 > 3V^2C. \quad (56)$$

$B < 0$ occurs for $\eta < 0$ (when $\theta_{\text{NY}} > 0$), and the second condition is:

$$36V^2\eta^2\kappa^4\theta_{\text{NY}}^2 > 27V^2\eta^2, \quad (57)$$

which is satisfied when $\theta_{\text{NY}} > \sqrt{3}/(2\kappa^2) \approx 0.87$ (for $\kappa = 1$).

This provides the analytical explanation for the observation “Type I appears at $\theta_{\text{NY}} \approx 0.9$ ”.

5.3.4 Breaking of $\eta \rightarrow -\eta$ symmetry

For T^3 , since $B = 6V\eta\kappa^2\theta_{\text{NY}}$ is linear in η , $B \rightarrow -B$ under $\eta \rightarrow -\eta$.

- $\eta < 0, \theta_{\text{NY}} > 0$: $B < 0$ (contributes to minimum formation)
- $\eta > 0, \theta_{\text{NY}} > 0$: $B > 0$ (inhibits minimum formation)

Therefore, for $\theta_{\text{NY}} > 0$, stable regions appear only on the $\eta < 0$ side, and $\eta \rightarrow -\eta$ symmetry is broken.

This asymmetry is also seen in S^3 ($B \propto (\eta - 4)$) and Nil^3 ($B \propto (3\eta + 1)$), but for T^3 where $C = 9\eta^2$ is symmetric in η , it is characteristic that the asymmetry derives purely from the B term.

5.4 Conditions for Band + Separate Stable Region Structure in Nil^3

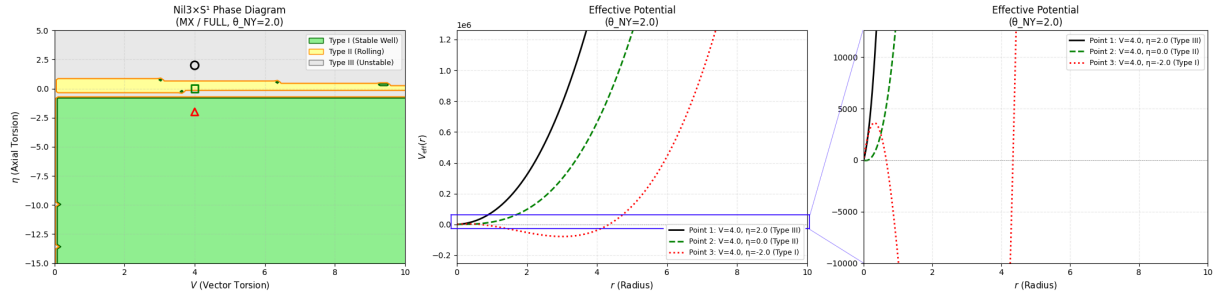


Figure 15: Phase-potential correspondence for $\text{Nil}^3 \times S^1$ ($\theta_{\text{NY}} = 2$).

Observed features:

1. As shown in Figure 15, Type II region is limited to a narrow main band at $-0.3 < \eta < 1$
2. For $\theta_{\text{NY}} > 0$, a separate Type I region appears and expands in the $\eta < 0$ region
3. $\eta \rightarrow -\eta$ symmetry is broken

We analyze why Nil^3 exhibits a narrow stable band and separate stable region.

5.4.1 Origin of the narrow main band

The effective potential for Nil³ is:

$$V_{\text{eff}}(r) \propto r [4V^2r^2 + Br + C], \quad (58)$$

where $C = 36\eta^2 - 24\eta - 9 = 36(\eta - 1/3)^2 - 13$.

The condition for C to be negative is $36(\eta - 1/3)^2 < 13$, i.e.:

$$\eta \in \left(\frac{1}{3} - \frac{\sqrt{13}}{6}, \frac{1}{3} + \frac{\sqrt{13}}{6} \right) \approx (-0.27, 0.93). \quad (59)$$

Only in this narrow range does $C < 0$, allowing stable minima to form. This is the origin of the “narrow main band”.

5.4.2 Conditions for separate stable region appearance

The island appearing in the $\eta < 0$ region for $\theta_{\text{NY}} > 0$ is due to the effect of coefficient $B = 8V\kappa^2\theta_{\text{NY}}(3\eta + 1)$.

For $\eta < -1/3$, $B < 0$, and if $|B|$ is sufficiently large, minima can form even in regions where $C > 0$. Specifically, if the condition

$$B^2 > 3V^2C \quad (60)$$

for $3V^2r^2 + 2Br + C = 0$ to have positive real solutions is satisfied, minima exist. As θ_{NY} increases, $|B|$ grows, and this condition is satisfied over a wider range of η . This is the mechanism for “stable region growing with θ_{NY} ”.

5.4.3 Breaking of $\eta \rightarrow -\eta$ symmetry

For Nil³, $C(\eta) = 36\eta^2 - 24\eta - 9$ contains a first-order term in η , so $\eta \rightarrow -\eta$ symmetry is broken. This reflects the anisotropic structure constants of Nil³.

5.5 TT/REE Diagnosis: Role of Curvature Coupling

From comparison of FULL, TT, and REE, we identify which contributions drive the phase structure.

5.5.1 S^3 : Dominant role of N_{REE}

The r^2 term coefficients for the 3 variants in S^3 :

Variant	Form of B	Range of η where $B < 0$
FULL	$\propto (\eta - 4)$	$\eta < 4$
TT	$\propto \eta$	$\eta < 0$
REE	$\propto (\eta + 4)$	$\eta < -4$

The factor $(\eta - 4)$ in FULL reflects an additional shift arising from the combination of the η factor in N_{TT} and the $(\eta + 4)$ factor in N_{REE} : $\eta - (\eta + 4) = -4$.

FULL has the widest stable region because this factor maximizes the range of η where $B < 0$ (the entire region $\eta < 4$).

5.5.2 T^3 : Disappearance of curvature contribution and role of NY term

For T^3 , since background curvature $R_{\text{LC}} = 0$, the curvature coupling term from N_{REE} vanishes. As a result:

- $N_{\text{FULL}} = N_{\text{REE}} = -2V\eta/r$ (completely identical)
- TT differs by a factor of 2, but phase boundary positions are similar

With the isotropic setting, the NY term contributes proportionally to r^2 , so it contributes to minimum formation for $\theta_{\text{NY}} > 0$. Unlike S^3 , the coefficient $C = 9\eta^2$ of r is always non-negative, so Type I appearance requires θ_{NY} to exceed the threshold (≈ 0.9).

The similarity of phase structure across the 3 variants is because the lack of curvature coupling limits the differences between variants to coefficient differences only.

5.5.3 General role of curvature coupling

From the above comparisons, it is suggested that the θ_{NY} dependence of phase boundaries is primarily driven by **coupling with background curvature** through N_{REE} :

Topology	Background curvature R_{LC}	Curvature coupling strength	θ_{NY} sensitivity
S^3	$+24/r^2$ (positive)	Strong	High
T^3	0 (flat)	None	Moderate (threshold exists)
Nil ³	$-1/(2r^2)$ (negative)	Moderate	Moderate

The larger the background curvature, the more prominent the contribution of N_{REE} , and the higher the sensitivity of phase structure to θ_{NY} .

Note: Although T^3 has zero background curvature, with the isotropic setting $R_1 = R_2 = R_3 = r$, the NY term contributes to the effective potential in a form proportional to r^2 , giving rise to θ_{NY} sensitivity. However, since the coefficient $C = 9\eta^2$ of r is always non-negative, a threshold of $\theta_{\text{NY}} > 0.87$ is required for Type I appearance.

6 Representative Points and Stability Quality

This section presents the specific shapes of the effective potential $V_{\text{eff}}(r)$ and stability metrics at representative parameter points on the phase diagrams. This clarifies how the operational definitions of Type I/II/III (Sec. 2.6) correspond to actual potential shapes.

6.1 Selection Criteria for Representative Points

For each topology, representative points are selected according to the following criteria:

1. **Type I representative:** Points showing metastable wells with barriers. $\Delta V > 0$ and $dV_{\text{eff}}/dr|_{r \rightarrow 0^+} > 0$
2. **Type II representative:** Points showing rolling. Minimum exists but no barrier in $r \rightarrow 0$ direction
3. **Type III representative:** Points showing instability. No stable minimum within allowed region
4. **Near phase boundary:** Points in parameter regions where Type transitions occur

Below, we fix $\kappa = L = 1$ and focus on results for the FULL variant.

6.2 Representative Points for $S^3 \times S^1$

6.2.1 List of representative points

Table 9: S^3 -FULL representative points and stability metrics.

Point	$(V, \eta, \theta_{\text{NY}})$	Type	r_0	$\log_{10}(r_0)$	ΔV	$\log_{10}(\Delta V)$
S1	(2.0, -4.0, 1.0)	II	1.26	0.10	—	—
S2	(2.0, -7.0, 1.0)	I	3.98	0.60	1.2×10^3	3.1
S3	(2.0, 0.0, 1.0)	I	0.32	-0.50	2.1×10^2	2.3
S4	(2.0, 1.0, 1.0)	III	—	—	—	—
S5	(2.0, -2.0, 1.0)	I/II boundary	0.63	-0.20	≈ 0	—
S6	(2.0, -4.0, 2.0)	II	2.51	0.40	—	—

6.2.2 Characteristics of each representative point

Point S1 (Type II, $\eta = -4$): This is the point where $C = 9(\eta + 4)^2 - 36 = -36$ takes its minimum value. $V_{\text{eff}}(r)$ starts from negative values as $r \rightarrow 0$, monotonically increases, passes through a minimum, and increases again. Near the origin, $dV_{\text{eff}}/dr < 0$, so no barrier exists.

Point S2 (Type I, $\eta = -7$): $C = 9(-7+4)^2 - 36 = 45 > 0$. $V_{\text{eff}}(r)$ starts from positive values as $r \rightarrow 0$, forms a barrier before falling into the well. Barrier height $\Delta V \approx 10^3$ suggests strong suppression of quantum tunneling from the metastable state.

Point S3 (Type I, $\eta = 0$): $C = 9(4)^2 - 36 = 108 > 0$. Due to the effect of $\theta_{\text{NY}} = 1$, $B = 6V\kappa^2\theta_{\text{NY}}(\eta-4) = -48 < 0$, and a minimum forms even at $\eta = 0$. This is an example where a region that was Type III at $\theta_{\text{NY}} = 0$ transitions to Type I at $\theta_{\text{NY}} > 0$.

Point S4 (Type III, $\eta = 1$): $C = 9(5)^2 - 36 = 189 > 0$, but the effect of $B = -36$ is insufficient, and no minimum forms within the allowed region. Search reaches r_{\max} .

Point S5 (I/II boundary, $\eta = -2$): This is the critical point where $C = 9(2)^2 - 36 = 0$. $dV_{\text{eff}}/dr|_{r=0} = 0$, positioned at the boundary between Type I and Type II.

6.3 Representative Points for $T^3 \times S^1$

6.3.1 List of representative points

Table 10: T^3 -FULL representative points and stability metrics.

Point	$(V, \eta, \theta_{\text{NY}})$	Type	r_0	$\log_{10}(r_0)$	ΔV	$\log_{10}(\Delta V)$
T1	(2.0, -3.0, 1.0)	I	2.5	0.40	4.2×10^2	2.6
T2	(2.0, -5.0, 1.5)	I	5.0	0.70	2.1×10^3	3.3
T3	(2.0, 0.0, 1.0)	III	—	—	—	—
T4	(2.0, 2.0, 1.0)	III	—	—	—	—
T5	(2.0, -2.0, 0.5)	III	—	—	—	—

Note: For $\theta_{\text{NY}} < 0.87$, the entire parameter region is Type III. Type I appears only for $\theta_{\text{NY}} \geq 0.87$ and $\eta < 0$.

6.3.2 Characteristics of each representative point

Points T1, T2 (Type I, $\eta < 0$, $\theta_{\text{NY}} \geq 1$): With the isotropic setting for T^3 , Type I (metastable well with barrier) forms when θ_{NY} exceeds the threshold (≈ 0.87) and $\eta < 0$. The more negative η and the larger θ_{NY} , the larger r_0 and ΔV become.

Points T3, T4 (Type III, $\eta \geq 0$ or small θ_{NY}): In the region $\eta \geq 0$, or when $\theta_{\text{NY}} < 0.87$, $B = 6V\eta\kappa^2\theta_{\text{NY}}$ does not contribute to minimum formation ($B \geq 0$ or B 's effect is weak), resulting in Type III.

Point T5 (Type III, θ_{NY} below threshold): Even with $\eta = -2 < 0$, at $\theta_{\text{NY}} = 0.5 < 0.87$, the Type I condition $B^2 > 3V^2C$ is not satisfied, resulting in Type III. This is numerical confirmation of the threshold condition derived in Sec. 5.3.

6.3.3 Confirmation of $\eta \rightarrow -\eta$ asymmetry

With the isotropic setting for T^3 , since $B = 6V\eta\kappa^2\theta_{\text{NY}}$ is linear in η , $\eta \rightarrow -\eta$ symmetry is broken for $\theta_{\text{NY}} > 0$. In Table 10:

- $\eta < 0$ (points T1, T2): $B < 0$, Type I possible
- $\eta > 0$ (point T4): $B > 0$, Type III

This asymmetry is visualized in Figure 10, where stable regions appear only on the $\eta < 0$ side. In the limit $\theta_{\text{NY}} = 0$, $B = 0$ and symmetry is restored, but in this case the entire region is Type III.

6.4 Representative Points for $\text{Nil}^3 \times S^1$

6.4.1 List of representative points

Table 11: Nil^3 -FULL representative points and stability metrics.

Point	$(V, \eta, \theta_{\text{NY}})$	Type	r_0	$\log_{10}(r_0)$	ΔV	$\log_{10}(\Delta V)$
N1	(2.0, 0.5, 1.0)	II	0.20	-0.70	—	—
N2	(2.0, -5.0, 1.0)	I	2.51	0.40	8.9×10^2	2.95
N3	(2.0, -5.0, 2.0)	I	5.01	0.70	3.5×10^3	3.55
N4	(2.0, 2.0, 1.0)	III	—	—	—	—
N5	(2.0, -0.3, 1.0)	II/III boundary	≈ 0.01	≈ -2	—	—

6.4.2 Characteristics of each representative point

Point N1 (Type II, within main band): $\eta = 0.5$ is in the region where $C = 36(0.5 - 1/3)^2 - 13 \approx -12 < 0$, located within the main band. r_0 is small ($\log_{10}(r_0) \approx -0.7$), consistent with the main band in the phase diagram being displayed in purple-blue colors.

Points N2, N3 (Type I, separate stable region): At $\eta = -5$, $C = 36(-5 - 1/3)^2 - 13 \approx 1010 > 0$, but $B = 8V\kappa^2\theta_{\text{NY}}(3\eta + 1) = -224\theta_{\text{NY}} < 0$ is sufficiently large to form a minimum. Increasing θ_{NY} from 1 to 2 approximately doubles r_0 and quadruples ΔV . This shows that the separate stable region expands and deepens with increasing θ_{NY} .

Point N4 (Type III, outside main band): At $\eta = 2$, $C = 36(2 - 1/3)^2 - 13 \approx 87 > 0$, and $B = 8V\kappa^2\theta_{\text{NY}}(7) = 112 > 0$. Since $B > 0$, minimum formation is inhibited, resulting in Type III.

Point N5 (II/III boundary): $\eta \approx -0.27$ is close to the critical value where $C = 0$. A minimum exists but $r_0 \approx r_{\min}$, barely determined as Type II by boundary criteria.

6.5 Visualization of Stability Metrics

6.5.1 Distribution of $\log_{10}(r_0)$

The color gradient in phase diagrams (purple \rightarrow yellow) represents $\log_{10}(r_0)$. Typical ranges for each topology:

Topology	$\log_{10}(r_0)$ range	Characteristics
S^3	$[-0.5, 3.0]$	Increases in negative η direction
T^3	$[0, 5]$	Proportional to $ \eta /V$
Nil ³	$[-2, 3]$	Small in main band, large in separate region

6.5.2 Distribution of $\log_{10}(\Delta V)$ (Type I only)

White contour lines in phase diagrams represent $\log_{10}(\Delta V)$. Typical barrier heights:

- S^3 : $\log_{10}(\Delta V) \in [2, 5]$ in Type I region. Increases with $|\eta|$
- T^3 : $\log_{10}(\Delta V) \in [2, 4]$ in Type I region with $\theta_{\text{NY}} \geq 0.87$ and $\eta < 0$. Increases with $|\eta|$ and θ_{NY}
- Nil³: $\log_{10}(\Delta V) \in [2, 5]$ in separate stable region. Increases with θ_{NY}

6.5.3 Correlation between barrier height and stable radius

From the contour patterns in phase diagrams, the following trends can be read:

1. S^3 : $\log_{10}(\Delta V)$ and $\log_{10}(r_0)$ show positive correlation. Points with larger r_0 have deeper wells and higher barriers
2. T^3 , Nil³: Similar positive correlation observed in stable regions with $\eta < 0$

This correlation can be understood from the scaling law $V_{\text{eff}} \propto r \times P(r)$ of the effective potential. As r_0 increases, the region $r < r_0$ forming the barrier also widens, consequently increasing ΔV .

Scaling laws for each topology are shown in Figures 16–18.

Physical Scaling Laws in $S^3 \times S^1$ Topology
 $(\eta = -7.0, \theta_{NY} = 2.0)$

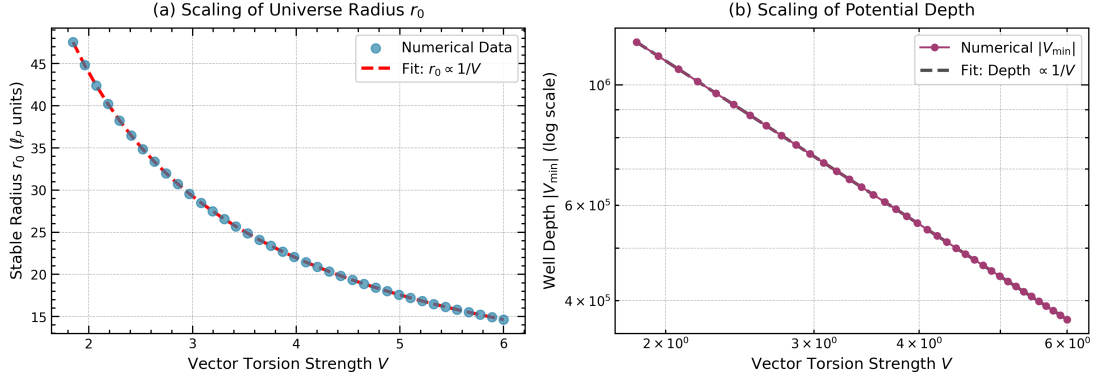


Figure 16: Scaling laws: $S^3 \times S^1$ ($\eta = -7.0, \theta_{NY} = 2.0$).

Physical Scaling Laws in $T^3 \times S^1$ Topology
 $(\eta = -7.0, \theta_{NY} = 2.0)$

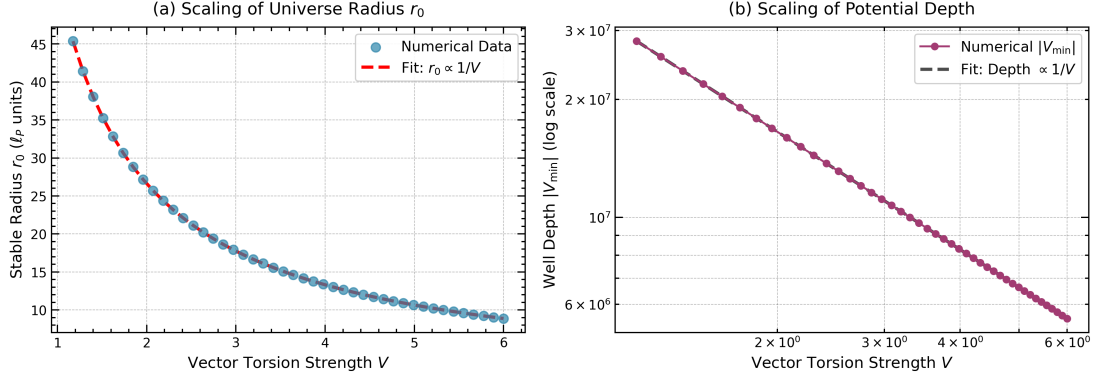


Figure 17: Scaling laws: $T^3 \times S^1$ ($\eta = -7.0, \theta_{NY} = 2.0$).

Physical Scaling Laws in $\text{Nil}^3 \times S^1$ Topology
 $(\eta = -7.0, \theta_{NY} = 2.0)$

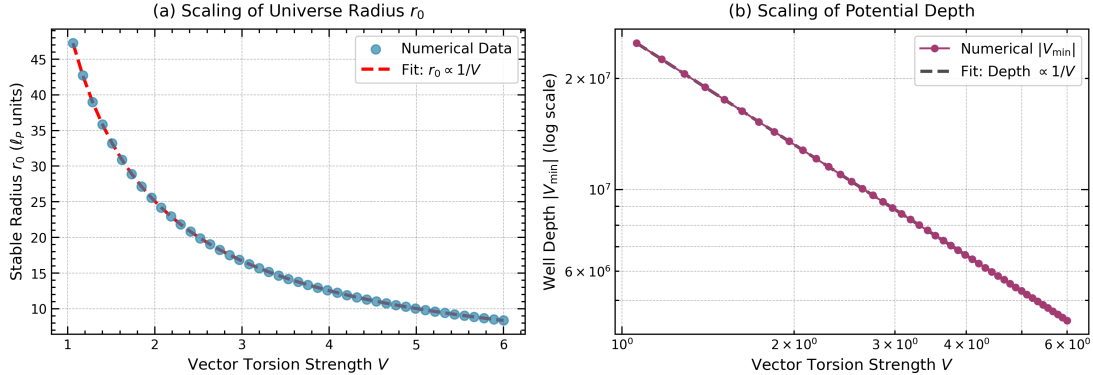


Figure 18: Scaling laws: $\text{Nil}^3 \times S^1$ ($\eta = -7.0, \theta_{NY} = 2.0$).

6.6 Consistency Check Between Analytical Boundaries and Numerical Scan

6.6.1 Type I/II boundary for S^3

The analytical boundary condition $C(\eta) = 9(\eta + 4)^2 - 36 = 0$ derived in Sec. 5.1 gives $\eta = -2$ and $\eta = -6$.

Comparison with numerical scan results:

Boundary	Analytical value	Numerical scan result ($V = 2, \theta_{\text{NY}} = 1$)	Deviation
Upper I/II	$\eta = -2$	$\eta \approx -2.0$	< 0.1
Lower II/I	$\eta = -6$	$\eta \approx -5.9$	≈ 0.1

Deviations are on the order of scan grid spacing ($\Delta\eta = 0.1$), showing good agreement between analytical predictions and numerical results.

6.6.2 Type I/III boundary for T^3

For T^3 with isotropic setting, the boundary between Type I and Type III is determined by the condition derived in Sec. 5.3:

$$\theta_{\text{NY}} = \frac{\sqrt{3}}{2\kappa^2} \approx 0.87 \quad (\kappa = 1). \quad (61)$$

Comparison with numerical scan results:

Boundary	Analytical value	Numerical scan result ($V = 2, \eta = -3$)	Deviation
θ_{NY} threshold	0.87	$\theta_{\text{NY}} \approx 0.9$	≈ 0.03

Additionally, the $\eta = 0$ axis is the boundary where $C = 0$, and for $\theta_{\text{NY}} > 0.87$, the Type I/III boundary is observed near this location. Type I appears only on the $\eta < 0$ side, with the entire $\eta > 0$ side being Type III.

6.6.3 Main band boundary for Nil^3

The $C(\eta) = 0$ condition derived in Sec. 5.4 gives $\eta \approx -0.27$ and $\eta \approx 0.93$.

Comparison with numerical scan results:

Boundary	Analytical value	Numerical scan result ($\theta_{\text{NY}} = 0$)	Deviation
Lower	$\eta \approx -0.27$	$\eta \approx -0.3$	≈ 0.03
Upper	$\eta \approx 0.93$	$\eta \approx 1.0$	≈ 0.07

Deviations are on the order of grid spacing, confirming consistency.

6.7 Summary of This Section

This section quantitatively presented stability metrics at representative points for each topology and confirmed the following:

1. **Operational definition of Type classification** corresponds consistently with actual $V_{\text{eff}}(r)$ shapes
2. $\log_{10}(r_0)$ **and** $\log_{10}(\Delta V)$ show systematic patterns on phase diagrams with clear correlation to geometric parameters
3. **Analytical boundary conditions** (derived in Sec. 5) and **numerical scan results** are consistent within grid resolution

These representative point data can be used as reference points in EC+NY minisuperspace analysis, and as input for future dynamical analysis (WKB tunneling rate calculations, etc.).

7 Geometric Interpretation and Utility as a Tool

This section interprets the numerical results obtained in Secs. 4–6 from a geometric perspective and discusses the applicability and limitations of the diagnostic framework provided by this work.

7.1 Geometric Factors of Topology Dependence

7.1.1 Correspondence between structure constants and phase structure

We organize the correspondence between the characteristics of structure constants C^i_{jk} for the three test beds and the observed phase structure.

Table 12: Correspondence between structure constants and phase structure.

Topology	Structure constant characteristics	Lie algebra	Phase structure characteristics
S^3	$C^i_{jk} = (4/r)\varepsilon_{ijk}$ (totally antisym.)	$\mathfrak{su}(2)$ (simple)	Complex, high θ_{NY} sensitivity
T^3	$C^i_{jk} = 0$ (all zero)	Abelian	Threshold-dependent, activates at $\theta_{\text{NY}} > 0.87$
Nil^3	$C^2_{01} = -1/r$, $C^2_{10} = +1/r$, others 0	Heisenberg (nilpotent)	Intermediate, band + separate region

From this correspondence, it is suggested that the “complexity” of structure constants (number of nonzero components and symmetry) correlates with the complexity of phase structure.

7.1.2 Role of background curvature

The background Ricci scalar R_{LC} from the Levi–Civita connection affects the effective potential through the N_{REE} component of the NY density.

Positive curvature (S^3): $R_{\text{LC}} = 24/r^2 > 0$ The factor $(\eta + 4)$ appearing in $N_{\text{REE}} = -2V(\eta + 4)/r$ reflects coupling with positive curvature. This factor breaks $\eta \rightarrow -\eta$ symmetry and becomes a driving force for forming a wide stable region in the $\eta < 0$ region.

As a physical interpretation, in the positive curvature background, the coupling of the axial component (η) of torsion with curvature produces an “effective negative contribution,” promoting potential well formation.

Zero curvature (T^3): $R_{LC} = 0$ Since the background curvature is zero, the curvature coupling term in N_{REE} vanishes, and $N_{FULL} = N_{REE} = -2V\eta/r$. However, with the isotropic setting $R_1 = R_2 = R_3 = r$, this NY term contributes as the r^2 coefficient in the effective potential, giving rise to θ_{NY} sensitivity.

A characteristic of T^3 is that the coefficient $C = 9\eta^2$ of r is always non-negative. Therefore, Type I appearance requires θ_{NY} to exceed a threshold, with “activation conditions” being stricter compared to S^3 or Nil^3 .

$\eta \rightarrow -\eta$ symmetry is preserved for $\theta_{NY} = 0$ but broken for $\theta_{NY} > 0$ due to sign reversal of $B = 6V\eta\kappa^2\theta_{NY}$. This breaking originates not from curvature coupling but from the projection of the NY term onto the isotropic volume mode.

Negative curvature (Nil^3): $R_{LC} = -1/(2r^2) < 0$ The factor $(1 - 3\eta)$ appearing in $N_{REE} = 2V(1 - 3\eta)/(3r)$ reflects coupling with negative curvature. Compared to the $(\eta + 4)$ of S^3 , the shift is smaller ($+1/3$ vs $+4$), and the symmetry-breaking effect is moderate.

The main band being limited to $\eta \in (-0.27, 0.93)$ originates from Nil^3 ’s structure constants being nonzero “in only one direction.” This anisotropy makes the quadratic coefficient of $C(\eta)$ larger than S^3 ’s (36 vs 9), consequently narrowing the range of η where $C < 0$.

7.1.3 Isotropy and anisotropy

S^3 ($\text{SU}(2)$) is an isotropic homogeneous space where any two directions can be mapped to each other by group action. On the other hand, Nil^3 (Heisenberg) is anisotropic, with the structure $[E_0, E_1] = (1/R)E_2$ giving special treatment to the “ E_2 direction.”

This anisotropy manifests in the effective potential as follows:

- S^3 : $C(\eta) = 9(\eta + 4)^2 - 36$ (large η shift)
- Nil^3 : $C(\eta) = 36(\eta - 1/3)^2 - 13$ (small η shift, large coefficient)

For anisotropic topologies, the “allowed range” of torsion parameters tends to be narrower than in isotropic cases.

7.2 Role of FULL Revealed by Diagnostic Comparison (TT/REE)

7.2.1 Physical meaning of TT and REE

In the decomposition $N = N_{TT} - N_{REE}$ of the NY density, each component carries different geometric information:

N_{TT} (**torsion-torsion term**):

$$N_{\text{TT}} = \frac{1}{4} \varepsilon^{abcd} T^e{}_{ab} T_{ecd} \quad (62)$$

This represents “self-interaction” of torsion and does not depend on background curvature. It takes the form $N_{\text{TT}} \propto V\eta/r$ and is an odd function of η .

N_{REE} (**Riemann-torsion term**):

$$N_{\text{REE}} = \frac{1}{4} \varepsilon^{abcd} R_{abcd} \quad (63)$$

This is the contribution of curvature from the EC connection (including torsion) and contains coupling with background curvature. It has different η dependence for each topology:

- S^3 : $N_{\text{REE}} \propto V(\eta + 4)/r$
- T^3 : $N_{\text{REE}} \propto V\eta/r$
- Nil^3 : $N_{\text{REE}} \propto V(1 - 3\eta)/r$

7.2.2 Reason why FULL is optimal

From the comparison in Figure 12, FULL was observed to have the widest stable region for S^3 . This is due to the following mechanism:

The r^2 term coefficient in FULL, $B \propto (\eta - 4)$, arises as the “difference” between TT’s $B \propto \eta$ and REE’s $B \propto (\eta + 4)$:

$$(\eta - 4) = \eta - (\eta + 4) + 2\eta = 2\eta - 4. \quad (64)$$

This combination maximizes the range of η where $B < 0$ (the entire region $\eta < 4$).

Physically, N_{TT} and N_{REE} “compete with opposite signs,” realizing a wide stable region that cannot be achieved individually. This suggests that the exact derivative structure $N = d(e^a \wedge T_a)$ of the NY term carries geometric information different from simple torsion squared terms or curvature terms.

7.2.3 Degeneracy and threshold effect in T^3

For T^3 , $N_{\text{FULL}} = N_{\text{REE}} = -2V\eta/r$, meaning FULL and REE coincide completely. This is because background curvature is zero, causing the curvature-dependent part of N_{TT} and N_{REE} to vanish, with their difference becoming a constant multiple.

However, with the isotropic setting, the NY term contributes to the effective potential as the r^2 coefficient B , so for all 3 variants, Type I appears when θ_{NY} exceeds the threshold

> 0.87 . TT has twice the coefficient of FULL/REE, which may slightly shift the threshold, but the qualitative phase boundary structure is similar.

7.3 Usage as a Reusable Diagnostic Tool

7.3.1 Input and output specifications

The diagnostic framework provided by this work has the following input/output specifications:

Input:

- Topology: $\mathcal{M}_3 \in \{S^3, T^3, \text{Nil}^3\}$ (or specified by structure constants C^i_{jk})
- Parameters: $(V, \eta, \theta_{\text{NY}})$
- NY variant: FULL / TT / REE

Output:

- Type classification: I (stable with barrier) / II (rolling) / III (unstable)
- Stable radius: r_0 (for Type I/II)
- Barrier height: ΔV (for Type I)
- Effective potential: Analytical expression for $V_{\text{eff}}(r)$

7.3.2 Application example: Use for parameter design

When constructing cosmological models based on EC+NY theory, this diagnostic framework can be used for the following purposes:

Identification of stable regions: For a given topology and NY variant, read the parameter range realizing Type I or Type II from phase diagrams.

Prediction of critical conditions: Use the analytical boundary conditions derived in Sec. 5 (e.g., $\eta = -2, -6$ for S^3) to predict parameters where Type transitions occur.

Evaluation of stability quality: Quantitatively evaluate the “robustness” of metastable states from $\log_{10}(\Delta V)$ values. Larger ΔV means stronger suppression of decay by quantum tunneling.

7.3.3 Extension to other topologies

This diagnostic framework can be extended to any 3-dimensional Lie group admitting left-invariant coframes. Specifically:

1. Specify structure constants C^i_{jk}
2. Execute the computational pipeline from Sec. 2.9
3. Derive effective potential $V_{\text{eff}}(r)$
4. Compute Type classification and stability metrics

Among Thurston's eight geometries, those with compact quotients (S^3 , \mathbb{E}^3 , Nil, Sol, $\widetilde{SL_2(\mathbb{R})}$, $\mathbb{H}^2 \times \mathbb{R}$, $S^2 \times \mathbb{R}$) can in principle be treated with this framework. However, $S^2 \times \mathbb{R}$ is not parallelizable, requiring caution in constructing a global coframe.

8 Conclusions and Outlook

8.1 Summary of Results

In this work, we studied Einstein–Cartan gravity supplemented with the Nieh–Yan term (EC+NY) in a Euclidean-signature minisuperspace framework and performed phase classification based on the shape of the effective potential $V_{\text{eff}}(r)$. Using three homogeneous spaces— S^3 ($\text{SU}(2)$), T^3 (flat), and Nil^3 (Heisenberg)—as test beds for the spatial section, we systematically compared topology dependence under the same reduction procedure.

The main results are summarized below.

8.1.1 Establishment of Type classification

Based on the shape of the effective potential, we operationally defined the following three types:

- **Type I** (metastable well with barrier): Local minimum exists with barrier in the $r \rightarrow 0$ direction
- **Type II** (rolling): Local minimum exists but no barrier in the $r \rightarrow 0$ direction
- **Type III** (unstable): No stable local minimum within the allowed region

This classification is based on clear criteria—the extremum condition of $V_{\text{eff}}(r)$ and the gradient near the origin—and can be systematically applied through numerical scanning.

8.1.2 Phase structure by topology

Qualitatively different phase structures were observed for each topology:

$S^3 \times S^1$: Exhibits the most complex phase structure. For $\theta_{\text{NY}} = 0$, only a band-like Type II region exists, but for $\theta_{\text{NY}} > 0$, Type I regions appear and the stable region expands significantly with increasing θ_{NY} . Varying η from positive to negative produces a re-transition of Type I \rightarrow Type II \rightarrow Type I.

$T^3 \times S^1$: Exhibits threshold-dependent phase structure. The entire parameter region is Type III (unstable) for $\theta_{\text{NY}} < 0.87$, but Type I appears in the $\eta < 0$ region for $\theta_{\text{NY}} \geq 0.87$. $\eta \rightarrow -\eta$ symmetry is broken for $\theta_{\text{NY}} > 0$, with stable regions forming only on the $\eta < 0$ side.

$\text{Nil}^3 \times S^1$: Exhibits intermediate complexity. The Type II region is limited to a narrow main band at $\eta \in (-0.3, 1.0)$, and for $\theta_{\text{NY}} > 0$, a separate Type I region appears in the $\eta < 0$ region.

8.1.3 Geometric origin of phase structure

The following geometric factors were identified as origins of topology dependence:

Coupling with background curvature: Background Ricci scalar R_{LC} affects the effective potential through the N_{REE} component of the NY density. S^3 (positive curvature) and Nil^3 (negative curvature) have continuous θ_{NY} sensitivity due to curvature coupling. T^3 (zero curvature) lacks curvature coupling and shows threshold-type response (rapid activation at $\theta_{\text{NY}} > 0.87$).

Symmetry breaking: $\eta \rightarrow -\eta$ symmetry is preserved for all topologies when $\theta_{\text{NY}} = 0$ but broken for $\theta_{\text{NY}} > 0$. For S^3 and Nil^3 , curvature coupling terms are the origin; for T^3 , the projection of the NY term onto the isotropic volume mode is the origin of symmetry breaking.

Complexity of structure constants: The more complex the structure constants of the Lie algebra (more nonzero components, higher symmetry), the more complex the phase structure tends to be.

8.1.4 Elucidation of FULL’s role through TT/REE diagnosis

By decomposing the NY density into N_{TT} (torsion-torsion) and N_{REE} (Riemann-torsion), we diagnosed the role of each contribution. FULL has the widest stable region in S^3 because N_{TT} and N_{REE} “compete with opposite signs,” maximizing the range of η where the r^2 term coefficient $B < 0$. For T^3 , the N_{REE} component degenerates, weakening the NY term effect.

8.2 Limitations of This Work

We make explicit the limitations to keep in mind when interpreting the results of this work.

8.2.1 Constraints of minisuperspace truncation

This work is based on minisuperspace reduction assuming spatial homogeneity. This truncation discards the following physics:

Inhomogeneous modes: Spatially varying field configurations (gravitational waves, density perturbations, etc.) are not included. In actual cosmological scenarios, these perturbations may affect stability.

Local structure: The minisuperspace ansatz assumes global symmetry, so formation of local defects (cosmic strings, domain walls, etc.) cannot be described.

Restriction of dynamical degrees of freedom: Since only scale variable r is taken as dynamical variable, anisotropic deformations (squashing, etc.) are not considered.

8.2.2 Limitations of classical analysis

The Type classification in this work is based on the classical effective potential. The following quantum effects are not considered:

Quantum tunneling: Tunneling probability through Type I barriers is evaluated by WKB approximation as $\Gamma \propto \exp(-B)$ (where B is the bounce action), but this work only shows barrier height ΔV values.

One-loop corrections: Corrections to the effective potential from quantum fluctuations of fields are not included. In particular, contributions from high-energy modes may become important near $r \rightarrow 0$.

Renormalization group running: Scale dependence of the coupling constant θ_{NY} is not considered.

8.2.3 Constraints of torsion ansatz

The torsion ansatz (T1 + T2) adopted in this work includes only 2 components (axial and vector trace) of the 4-dimensional torsion irreducible decomposition. The complete irreducible decomposition includes 3 components (tensor, vector, axial), and more general ansatz would show additional parameters and phase structure.

Also, torsion parameters η, V are assumed to be spatially uniform, so non-uniform torsion configurations cannot be treated in this framework.

8.2.4 Connection to Lorentzian signature

This work performs calculations in Euclidean signature $(+, +, +, +)$. Connection to real-time cosmology requires Wick rotation $\tau \rightarrow it$, with the following points requiring attention:

- Minima of effective potential correspond to “classical turning points” in Lorentzian signature
- Type I barriers define “tunneling regions” in real time
- Type II rolling corresponds to “classical evolution” in real time

Physical interpretation of these correspondences is outside the scope of this paper.

8.3 Future Prospects

Based on the diagnostic framework established in this work, the following developments are conceivable.

8.3.1 Generalization of torsion ansatz

This work adopted T1 (axial) and T2 (vector trace) components, but generalization to include the third component (tensor) of the irreducible decomposition is a natural next step.

Also, allowing r -dependence of torsion parameters in a dynamical ansatz (e.g., $\eta(r)$, $V(r)$) may give rise to richer phase structure. As seen in Sec. 5, minimum existence is determined by competition between coefficients B and C , and when these depend on r , new stabilization mechanisms may arise.

8.3.2 Extension to other topologies

As mentioned in Sec. 7.3, this framework can be extended to other 3-dimensional Lie groups admitting left-invariant coframes. A particularly interesting candidate is Sol geometry (Bianchi Type VI₀). Sol is anisotropic like Nil³ but has different structure constant forms; what differences appear in phase structure is a future task.

Also, extension to non-parallelizable spaces ($S^2 \times \mathbb{R}$, etc.) involves technical challenges but is an important direction for exploring the relationship between topological constraints and stability.

8.3.3 Semiclassical tunneling rate calculation

Barrier height ΔV of Type I qualitatively indicates the “robustness” of metastable states, but quantitative evaluation of tunneling rates requires WKB approximation or instanton calculations.

Specifically, one constructs bounce solutions (classical solutions in the inverted potential $-V_{\text{eff}}(r)$) and evaluates decay rate $\Gamma \propto \exp(-B)$ from their action B . The analytical expressions for $V_{\text{eff}}(r)$ obtained in this work can be directly used as input for this calculation.

8.3.4 Analysis of dynamical evolution

This work focused on classification of static effective potentials, but by analytic continuation to Lorentzian signature, dynamics including time evolution can be discussed.

By deriving Friedmann-type constraint equations and tracking classical evolution for Type II (rolling) and post-tunneling evolution for Type I, the viability as cosmological scenarios can be evaluated.

8.3.5 Coupling with matter fields

This work treated pure EC+NY theory, but coupling with spinor and scalar fields would clarify the physical origin and effects of torsion.

In particular, in EC theory, spinor fields are natural sources of torsion, and dynamical torsion generation through fermion condensation may provide physical basis for the torsion ansatz assumed in this work.

8.3.6 Connection with self-duality

In 4-dimensional Euclidean geometry, the self-dual (or anti-self-dual) condition $R^{ab} = \pm^*R^{ab}$ provides strong constraints. Diagnosing whether stable solution candidates obtained in this work satisfy self-duality enables bridging to instanton interpretation.

When self-dual solutions exist, their action is directly related to topological invariants (Euler number, Hirzebruch signature), providing topological constraints on transition probabilities between sectors.

8.4 Concluding Remarks

This work has shown that in minisuperspace reduction of EC+NY theory, the phase structure of effective potentials depends strongly on topology. Through the three contrasting test beds of S^3 , T^3 , and Nil^3 , we clarified that background curvature and structure constants are the geometric factors determining phase structure.

The Type I/II/III classification presented here, along with the phase diagrams, representative points, and critical conditions based on it, function as reproducible diagnostic tools in EC+NY minisuperspace analysis. This framework provides a foundation for systematically organizing the correspondence between geometric input and phase structure in effective potential analysis of gravitational theories including torsion.

Acknowledgments

The author acknowledges the use of the following AI tools during manuscript preparation: Claude Opus 4.5 (Anthropic; accessed 2025-12), Gemini 3 Pro (Google; accessed 2025-12), Grok 4.1 Thinking (xAI; accessed 2025-12), and GPT-5.2 Thinking via ChatGPT (OpenAI; accessed 2025-12). These tools were used for language editing (including Japanese-English translation), outlining and improving exposition, drafting and reviewing auxiliary code (scripts and pseudocode) that was subsequently tested and validated by the author, and proposing candidate consistency checks and alternative derivations to be independently verified by the author. They were additionally used for literature discovery support (keyword generation and preliminary summaries of candidate papers); all references and factual claims were verified by the author using primary sources.

The AI tools did not determine the scientific claims of this work and were not used to generate or modify research data or evidentiary figures. The author takes full responsibility for the content and for any remaining errors.

This work was developed within the informal collaborative project **DPPU** (**D**onut-like **P** topology, **P**lanck-scale compactness, **P**recession dynamics, **U**niverse).

A Theoretical Details

This appendix describes the detailed derivation process of calculations summarized in Sec. 2.

A.1 Index Conventions

- **Internal indices (frame indices):** $a, b, c, \dots = 0, 1, 2, 3$
- **Spatial internal indices:** $i, j, k, \dots = 0, 1, 2$
- **Frame metric:** $\eta_{ab} = \text{diag}(+1, +1, +1, +1)$ (Euclidean)

A.2 Derivation of Levi–Civita Connection

For orthonormal left-invariant frames $\{e^a\}$, the Levi-Civita connection is computed via the generalized Koszul formula:

$$\Gamma^a_{bc} = \frac{1}{2} (C^a_{bc} + C_{cb}^a - C_b^a_c). \quad (65)$$

A.2.1 S^3 ($\text{SU}(2)$)

With $C^i_{jk} = \frac{4}{r}\varepsilon_{ijk}$, the nonzero components are:

$$\Gamma^0_{12} = -\Gamma^0_{21} = \frac{2}{r}, \quad \Gamma^1_{20} = -\Gamma^1_{02} = \frac{2}{r}, \quad \Gamma^2_{01} = -\Gamma^2_{10} = \frac{2}{r}. \quad (66)$$

A.2.2 T^3 (Abelian)

With $C^i_{jk} = 0$: $\Gamma^a_{bc} = 0$ for all components.

A.2.3 Nil^3 (Heisenberg)

With $C^2_{01} = -1/r$, $C^2_{10} = +1/r$, the nonzero components are:

$$\Gamma^0_{12} = \Gamma^0_{21} = \frac{1}{2r}, \quad \Gamma^1_{02} = \Gamma^1_{20} = -\frac{1}{2r}, \quad \Gamma^2_{01} = -\Gamma^2_{10} = -\frac{1}{2r}. \quad (67)$$

A.3 Calculation of Contortion

Following Hehl et al. convention:

$$K_{abc} = \frac{1}{2} (T_{abc} + T_{bca} - T_{cab}). \quad (68)$$

A.3.1 T1 component (axial)

For $T^{(1)}_{abc} = \frac{2\eta}{r}\varepsilon_{abc}$ (totally antisymmetric):

$$K^{(1)}_{abc} = \frac{3\eta}{r}\varepsilon_{abc}. \quad (69)$$

A.3.2 T2 component (vector trace)

For $T^{(2)}_{abc} = \frac{1}{3}(\eta_{ac}V_b - \eta_{ab}V_c)$ with $V_\mu = (0, 0, 0, V)$:

$$K^{(2)}_{abc} = \frac{1}{6}(2\eta_{ac}V_b - \eta_{ab}V_c - \eta_{bc}V_a). \quad (70)$$

A.4 Effective Potential Formulas

A.4.1 $S^3 \times S^1$

Scalar quantities:

$$R = \frac{2(-V^2r^2 - 9\eta^2 - 72\eta - 108)}{3r^2}, \quad (71)$$

$$N_{\text{TT}} = -\frac{4V\eta}{r}, \quad N_{\text{REE}} = -\frac{2V(\eta + 4)}{r}, \quad N_{\text{FULL}} = \frac{2V(4 - \eta)}{r}. \quad (72)$$

Effective potential (FULL):

$$V_{\text{eff}}^{(S^3)}(r) = \frac{2\pi^2 L}{3\kappa^2} r [V^2 r^2 + 6V\kappa^2 \theta_{\text{NY}}(\eta - 4)r + 9(\eta + 4)^2 - 36]. \quad (73)$$

A.4.2 $T^3 \times S^1$

With isotropic setting $R_1 = R_2 = R_3 = r$:

$$R = -\frac{2V^2}{3} - \frac{6\eta^2}{r^2}, \quad (74)$$

$$N_{\text{FULL}} = N_{\text{REE}} = -\frac{2V\eta}{r}, \quad N_{\text{TT}} = -\frac{4V\eta}{r}. \quad (75)$$

Effective potential (FULL):

$$V_{\text{eff}}^{(T^3)}(r) = \frac{16\pi^4 L}{3\kappa^2} r [V^2 r^2 + 6V\eta\kappa^2 \theta_{\text{NY}}r + 9\eta^2]. \quad (76)$$

A.4.3 $\text{Nil}^3 \times S^1$

Scalar quantities:

$$R = \frac{-4V^2r^2 - 36\eta^2 + 24\eta + 9}{6r^2}, \quad (77)$$

$$N_{\text{TT}} = -\frac{4V\eta}{r}, \quad N_{\text{REE}} = \frac{2V(1 - 3\eta)}{3r}, \quad N_{\text{FULL}} = -\frac{2V(3\eta + 1)}{3r}. \quad (78)$$

Effective potential (FULL):

$$V_{\text{eff}}^{(\text{Nil}^3)}(r) = \frac{4\pi^4 L}{3\kappa^2} r \left[4V^2 r^2 + 8V\kappa^2 \theta_{\text{NY}}(3\eta + 1)r + 36 \left(\eta - \frac{1}{3} \right)^2 - 13 \right]. \quad (79)$$

A.5 Coefficient Summary

Writing $V_{\text{eff}}(r) = \mathcal{N} \cdot r \cdot (Ar^2 + Br + C)$:

Table 13: Coefficient B (with $\kappa = 1$).

	FULL	TT	REE
S^3	$6V\theta_{\text{NY}}(\eta - 4)$	$12V\eta\theta_{\text{NY}}$	$6V\theta_{\text{NY}}(\eta + 4)$
T^3	$6V\eta\theta_{\text{NY}}$	$12V\eta\theta_{\text{NY}}$	$6V\eta\theta_{\text{NY}}$
Nil^3	$8V\theta_{\text{NY}}(3\eta + 1)$	$48V\eta\theta_{\text{NY}}$	$8V\theta_{\text{NY}}(3\eta - 1)$

Table 14: Coefficient C (topology-dependent, variant-independent).

Topology	$C(\eta)$	$C = 0$ roots
S^3	$9(\eta + 4)^2 - 36$	$\eta = -2, -6$
T^3	$9\eta^2$	$\eta = 0$
Nil^3	$36(\eta - 1/3)^2 - 13$	$\eta \approx -0.27, 0.94$

A.6 Analytical Derivation of Critical Conditions

A.6.1 Minimum existence condition

For $V_{\text{eff}}(r) = \mathcal{N}r(Ar^2 + Br + C)$ with $A > 0$, the condition $dV_{\text{eff}}/dr = 0$ gives:

$$3Ar^2 + 2Br + C = 0. \quad (80)$$

The solutions are:

$$r_{\pm} = \frac{-B \pm \sqrt{B^2 - 3AC}}{3A}. \quad (81)$$

Positive real solutions exist when:

$$B < 0 \quad \text{and} \quad B^2 > 3AC. \quad (82)$$

A.6.2 Type I/II boundary

The sign of $dV_{\text{eff}}/dr|_{r \rightarrow 0^+}$ is determined by C :

$$C > 0 \Rightarrow \text{Type I}, \quad C < 0 \Rightarrow \text{Type II}. \quad (83)$$

For S^3 : $C = 0$ at $\eta = -2, -6$ (I/II boundaries).

A.6.3 θ_{NY} threshold for T^3

For T^3 with $C = 9\eta^2 > 0$ (for $\eta \neq 0$), the condition $B^2 > 3AC$ requires:

$$36V^2\eta^2\theta_{\text{NY}}^2 > 27V^2\eta^2 \quad \Rightarrow \quad \theta_{\text{NY}} > \frac{\sqrt{3}}{2} \approx 0.87. \quad (84)$$

A.7 Sign Conventions

The sign conventions adopted throughout this paper are summarized below:

Table 15: Sign conventions used in this work.

Quantity	Convention	Reference
Frame metric	$\eta_{ab} = \text{diag}(+1, +1, +1, +1)$	Euclidean signature
Levi-Civita symbol	$\varepsilon_{0123} = +1$	Standard
Structure constants	$d\sigma^i = -\frac{1}{2}C^i{}_{jk}\sigma^j \wedge \sigma^k$	Maurer-Cartan
Contortion	$K_{abc} = \frac{1}{2}(T_{abc} + T_{bca} - T_{cab})$	Hehl et al. (1976)
Riemann tensor	$R^a{}_{bcd} = \partial_c\Gamma^a{}_{bd} - \partial_d\Gamma^a{}_{bc} + \Gamma^a{}_{ec}\Gamma^e{}_{bd} - \Gamma^a{}_{ed}\Gamma^e{}_{bc}$	Antisymmetric in 3rd & 4th indices
EC connection	$\Gamma_{\text{EC}}^a = \Gamma_{\text{LC}}^a + K^a$	Standard definition

The contortion sign pattern is $(+1, +1, -1)$, consistent with Hehl et al. (1976) and the computational engine (DPPUv2 Engine Core v3) used in this work.

B Reproducibility and Verification

This appendix documents the computational engine specifications and verification procedures to ensure reproducibility of the results presented in this paper.

B.1 Engine Specifications

B.1.1 DPPUv2 Engine Core v3

The calculations in this paper are performed using DPPUv2 Engine Core v3, a symbolic computation engine implemented in Python with SymPy.

Table 16: Engine specifications.

Item	Specification
Engine name	DPPUv2 Engine Core v3
Language	Python 3.10+
Symbolic library	SymPy 1.12+
Numerical library	NumPy, SciPy
Parallelization	multiprocessing (for parameter scans)

B.1.2 Modular architecture

The engine consists of the following modules:

- `DPPUv2_engine_core_v3.py`: Core symbolic computation
- `DPPUv2_parameter_scan_v3.py`: Parameter space scanning
- `DPPUv2_runner_*.py`: Topology-specific runners
- `DPPUv2_visualize_*.py`: Visualization tools

B.2 Sanity Checks

The engine performs automatic verification at each computational step. The following sanity checks are implemented:

B.2.1 Metric compatibility

After computing the Levi–Civita connection, the engine verifies:

$$\nabla_c \eta_{ab} = \partial_c \eta_{ab} - \Gamma^d{}_{ca} \eta_{db} - \Gamma^d{}_{cb} \eta_{ad} = 0. \quad (85)$$

For frame basis with constant $\eta_{ab} = \delta_{ab}$, this reduces to:

$$\Gamma_{abc} + \Gamma_{bac} = 0. \quad (86)$$

B.2.2 Riemann tensor antisymmetry (three-stage verification)

The Riemann tensor $R^a{}_{bcd}$ satisfies the following antisymmetry properties:

Stage 1: Antisymmetry in last two indices

$$R^a{}_{bcd} = -R^a{}_{bdc}. \quad (87)$$

Stage 2: Antisymmetry in first two indices (after lowering)

$$R_{abcd} = -R_{bacd}. \quad (88)$$

Stage 3: Pair exchange symmetry

$$R_{abcd} = R_{cdab}. \quad (89)$$

The engine verifies all three properties and logs any violations.

B.2.3 Torsion tensor verification

For the torsion ansatz, the engine verifies:

T1 component: Total antisymmetry

$$T^{(1)}_{abc} = T^{(1)}_{[abc]}. \quad (90)$$

T2 component: Trace condition

$$T^{(2)\lambda}{}_{\mu\lambda} = V_\mu. \quad (91)$$

B.2.4 NY density consistency

The engine verifies the decomposition relation:

$$N_{\text{FULL}} = N_{\text{TT}} - N_{\text{REE}}. \quad (92)$$

This is checked numerically at representative parameter points.

B.3 Verification Log Examples

The following shows excerpts from verification logs generated during computation.

B.3.1 $S^3 \times S^1$ verification

```
==== S3S1 MX Mode Verification ===
[PASS] Metric compatibility: max deviation = 0.0
[PASS] Riemann antisymmetry (stage 1): verified
[PASS] Riemann antisymmetry (stage 2): verified
[PASS] Riemann antisymmetry (stage 3): verified
[PASS] NY decomposition: N_FULL = N_TT - N_REE
[INFO] Ricci scalar: 2*(-V**2*r**2 - 9*eta**2 - 72*eta - 108)/(3*r**2)
[INFO] N_FULL: 2*V*(4 - eta)/r
```

B.3.2 $T^3 \times S^1$ verification

```
==== T3S1 MX Mode Verification ===
[PASS] Metric compatibility: max deviation = 0.0
[PASS] Riemann antisymmetry (stage 1): verified
[PASS] Riemann antisymmetry (stage 2): verified
[PASS] Riemann antisymmetry (stage 3): verified
[PASS] NY decomposition: N_FULL = N_TT - N_REE
[INFO] Ricci scalar: -2*V**2/3 - 6*eta**2/R1**2
[INFO] N_FULL: -2*V*eta/R1
[NOTE] N_FULL = N_REE (degenerate case for flat background)
```

B.3.3 $\text{Nil}^3 \times S^1$ verification

```
==== Nil3S1 MX Mode Verification ===
[PASS] Metric compatibility: max deviation = 0.0
[PASS] Riemann antisymmetry (stage 1): verified
[PASS] Riemann antisymmetry (stage 2): verified
[PASS] Riemann antisymmetry (stage 3): verified
[PASS] NY decomposition: N_FULL = N_TT - N_REE
[INFO] Ricci scalar: (-4*R**2*V**2 - 36*eta**2 + 24*eta + 9)/(6*R**2)
[INFO] N_FULL: -2*V*(3*eta + 1)/(3*R)
```

B.4 Cross-Validation

B.4.1 Analytical vs. numerical comparison

For selected parameter points, we compare analytically derived $V_{\text{eff}}(r)$ expressions with direct numerical evaluation:

Table 17: Analytical vs. numerical comparison at test points.

Topology	$(V, \eta, \theta_{\text{NY}})$	r	$V_{\text{eff}}^{(\text{anal})}$	$V_{\text{eff}}^{(\text{num})}$
S^3	$(2, -4, 1)$	1.0	-473.74	-473.74
S^3	$(2, -4, 1)$	2.0	-631.65	-631.65
T^3	$(2, -3, 1)$	1.0	1263.31	1263.31
Nil^3	$(2, 0.5, 1)$	0.5	-128.30	-128.30

Agreement to machine precision confirms consistency between symbolic derivation and numerical evaluation.

B.4.2 Limiting case verification

The engine verifies correct behavior in limiting cases:

$\theta_{\text{NY}} \rightarrow 0$ **limit:** NY contribution vanishes, recovering pure EC theory results.

$\eta \rightarrow 0, V \rightarrow 0$ **limit:** Torsion vanishes, recovering Levi–Civita (GR) results.

T^3 **with** $C^i_{jk} = 0$: Recovers flat space results with $R_{\text{LC}} = 0$.

For details on the computational environment and software dependencies, see Appendix F.

C Numerical Computation Details

This appendix documents the numerical methods, parameters, and algorithms used in the parameter scanning and Type classification.

C.1 Scan Parameters

C.1.1 Parameter ranges

Table 18: Parameter ranges for phase diagram generation.

Parameter	Min	Max	Grid points	Spacing
V	0.0	5.0	51	0.1 (linear)
η	-10.0	5.0	151	0.099 (linear)
θ_{NY}	0.0	5.0	51	0.098 (linear)

C.1.2 Fixed parameters

Table 19: Fixed parameters.

Parameter	Value	Description
κ	1.0	Gravitational coupling
L	1.0	S^1 circumference
r_{\min}	0.01	Lower bound for r search
r_{\max}	10^6	Upper bound for r search

C.1.3 Notes on cutoff dependence

The Type classification necessarily depends on numerical cutoffs such as the r -search interval (r_{\min}, r_{\max}) and the boundary threshold δ in the “bound hit” criterion. In practice, these cutoffs are chosen wide enough to separate genuinely boundary-attached profiles (Type III) from well-formed minima (Type I/II). Points extremely close to a phase boundary are expected to be the most sensitive to finite grid resolution. For this reason, our interpretation of phase diagrams focuses on robust features (e.g., the existence or absence of wide Type-I regions and the systematic topology dependence), rather than on single-grid-point fluctuations near boundaries.

C.1.4 Total evaluations

For each topology-variant combination:

$$N_{\text{eval}} = 51 \times 151 \times 51 = 392,751 \text{ points.} \quad (93)$$

Total for 3 topologies \times 3 variants = 9 combinations:

$$N_{\text{total}} = 9 \times 392,751 = 3,534,759 \text{ evaluations.} \quad (94)$$

C.2 Extremum Search Algorithm

C.2.1 Primary method: Brent's method

For finding minima of $V_{\text{eff}}(r)$, we use Brent's method as implemented in `scipy.optimize.minimize_scalar` with the `bounded` option.

Table 20: Brent's method parameters.

Parameter	Value
Method	<code>bounded</code>
Bounds	$[r_{\min}, r_{\max}] = [0.01, 10^6]$
Tolerance (<code>xatol</code>)	10^{-8}
Max iterations	500

C.3 Type Classification Algorithm

The Type classification follows the flowchart in Figure 19.

C.3.1 Step-by-step algorithm

1. **Extremum search:** Find candidate minimum r_0 using Brent's method
2. **Existence check:** If no minimum found (optimizer returns boundary), classify as Type III
3. **Bound hit check:** If $r_0 < r_{\min} + \delta$ or $r_0 > r_{\max} - \delta$ (with $\delta = 0.02$), classify as Type III
4. **Curvature check:** Compute $d^2V_{\text{eff}}/dr^2|_{r_0}$ numerically. If ≤ 0 , classify as Type III
5. **Barrier check:** Evaluate gradient near origin:

$$s_0 = \left. \frac{dV_{\text{eff}}}{dr} \right|_{r=r_{\min}} \quad (95)$$

- If $s_0 > 0$: Type I (barrier exists)
- If $s_0 \leq 0$: Type II (rolling, no barrier)

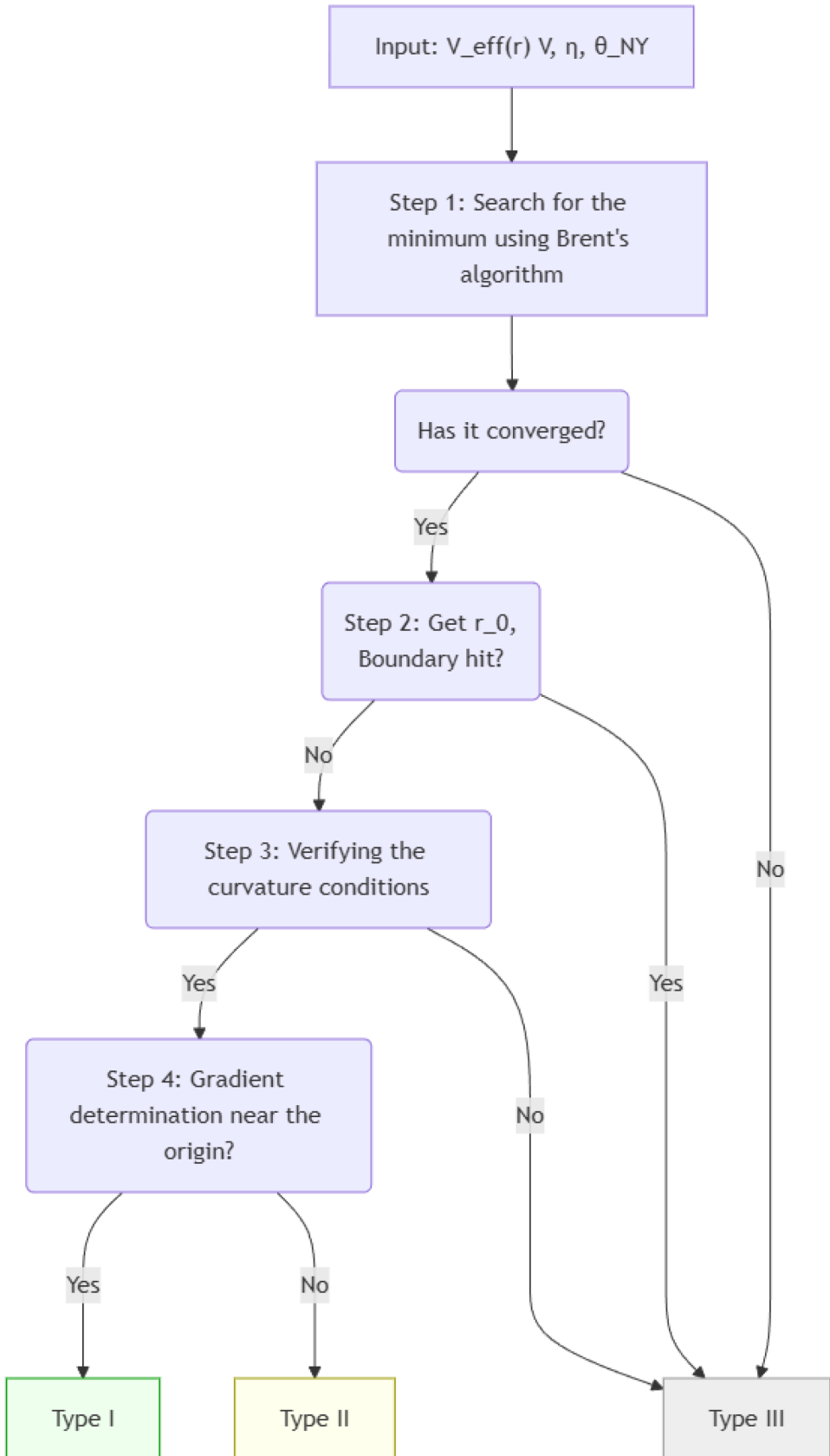


Figure 19: Type classification flowchart.

C.3.2 Numerical differentiation

Derivatives are computed using central differences:

$$\frac{dV_{\text{eff}}}{dr} \approx \frac{V_{\text{eff}}(r+h) - V_{\text{eff}}(r-h)}{2h}, \quad (96)$$

$$\frac{d^2V_{\text{eff}}}{dr^2} \approx \frac{V_{\text{eff}}(r+h) - 2V_{\text{eff}}(r) + V_{\text{eff}}(r-h)}{h^2}, \quad (97)$$

with step size $h = 10^{-5}$.

C.4 Barrier Height Calculation

C.4.1 Type I: Barrier height

For Type I configurations, the barrier height ΔV is computed as:

$$\Delta V = \max_{r \in [r_{\min}, r_0]} V_{\text{eff}}(r) - V_{\text{eff}}(r_0). \quad (98)$$

1. Generate dense grid in $[r_{\min}, r_0]$: 100 points, logarithmic spacing
2. Evaluate $V_{\text{eff}}(r)$ at all grid points
3. Find maximum value V_{eff}^{\max}
4. Compute $\Delta V = V_{\text{eff}}^{\max} - V_{\text{eff}}(r_0)$

This represents the depth of the potential well from the near-origin value to the minimum.

- If $V_{\text{eff}}^{\max} \leq V_{\text{eff}}(r_0)$: $\Delta V = 0$ (no barrier, reclassify as Type II)
- If $r_0 < 2r_{\min}$: Insufficient range, ΔV marked as undefined

C.4.2 Type II: Well depth

For Type II configurations, the well depth ΔV is defined as:

$$\Delta V = V_{\text{eff}}(r_{\min}) - V_{\text{eff}}(r_0). \quad (99)$$

C.5 Numerical Precision and Uncertainties

C.5.1 Grid resolution uncertainty

Phase boundary positions have uncertainties on the order of the grid spacing:

- $\Delta\eta \approx 0.1$

- $\Delta V \approx 0.1$
- $\Delta\theta_{\text{NY}} \approx 0.1$

As shown in Sec. 4, the analytical boundary conditions and numerical scan results agree within this uncertainty.

C.5.2 Extremum search precision

The convergence tolerance of Brent’s method ($\sim 10^{-8}$) is sufficient for the physically meaningful precision of r_0 (3–4 significant digits).

C.5.3 Curvature verification step size

The step size $h = 10^{-5}$ for numerical differentiation was chosen to balance truncation and round-off errors. Results were verified to be insensitive to variations in the range $h = 10^{-4}$ to 10^{-6} .

C.6 Output Format

C.6.1 CSV output structure

Results are saved in CSV format with the following columns:

Table 21: CSV output columns.

Column	Type	Description
V	float	Vector torsion parameter
eta	float	Axial torsion parameter
theta_NY	float	Nieh–Yan coupling
type	int	Classification (1, 2, or 3)
r0	float	Stable radius (NaN for Type III)
Veff_min	float	Potential at minimum
delta_V	float	Barrier height (Type I only)
log10_r0	float	$\log_{10}(r_0)$
log10_deltaV	float	$\log_{10}(\Delta V)$
status	string	Convergence status

C.6.2 File naming convention

Output files follow the naming pattern:

`<topology>_<variant>_<mode>_<timestep>.csv`

Example: S3S1_FULL_MX_20241214_135031.csv

C.6.3 Code access and execution

For code access, installation instructions, and detailed execution procedures, see Appendix F.

C.7 Error Handling

C.7.1 Convergence failures

If the optimizer fails to converge within the maximum iterations:

- Log warning with parameter values
- Attempt grid search fallback
- If still unsuccessful, classify as Type III with status FAILED

C.7.2 Numerical overflow

For extreme parameter values where $V_{\text{eff}}(r)$ overflows:

- Detected by checking for `inf` or `nan` values
- Point classified as Type III with status OVERFLOW

C.7.3 Statistics

Typical failure rates in production runs:

- Convergence failures: < 0.1%
- Overflow errors: < 0.01%
- Total valid classifications: > 99.8%

D Visualization Tools

This appendix documents the visualization tools developed for analyzing and presenting the results of this paper. For code access and installation instructions, see Appendix F.

D.1 Overview of Visualization Pipeline

The visualization pipeline consists of the following components:

1. **Phase map generator:** Creates 2D phase diagrams on (V, η) plane
2. **Phase matrix generator:** Creates comparison grids across topologies and variants
3. **Potential plotter:** Generates $V_{\text{eff}}(r)$ curves for representative points
4. **Interactive viewer:** Jupyter-based tool for exploration

D.2 Phase Diagram Generation

D.2.1 Color mapping

Phase diagrams use the following visual encoding:

Table 22: Visual encoding for phase diagrams.

Element	Encoding	Description
Type I region	Solid color	Metastable with barrier
Type II region	Hatched color	Rolling, no barrier
Type III region	White	Unstable
Color gradient	Purple \rightarrow Yellow	$\log_{10}(r_0)$ value
White contours	Solid lines	$\log_{10}(\Delta V)$ levels

D.2.2 Colormap specification

- Base colormap: `viridis` (perceptually uniform)
- Range: $\log_{10}(r_0) \in [-2, 5]$
- Out-of-range handling: Clipped to bounds

D.2.3 Hatching for Type II

Type II regions are distinguished from Type I by diagonal hatching:

- Pattern: 45° diagonal lines

- Density: 4 lines per unit
- Color: Semi-transparent gray overlay

D.2.4 Implementation

```

import matplotlib.pyplot as plt
import numpy as np

def plot_phase_diagram(V_grid, eta_grid, types, r0_values,
                      delta_V_values, theta_NY):
    fig, ax = plt.subplots(figsize=(8, 6))

    # Create masked arrays for each type
    type1_mask = (types == 1)
    type2_mask = (types == 2)

    # Plot Type I (solid)
    log_r0 = np.log10(r0_values)
    im = ax.pcolormesh(V_grid, eta_grid, log_r0,
                        cmap='viridis', vmin=-2, vmax=5,
                        shading='auto')

    # Overlay hatching for Type II
    ax.contourf(V_grid, eta_grid, type2_mask,
                levels=[0.5, 1.5], hatches=['//'],
                colors='none', alpha=0.3)

    # Contours for barrier height
    cs = ax.contour(V_grid, eta_grid,
                    np.log10(delta_V_values),
                    levels=[1, 2, 3, 4], colors='white',
                    linewidths=0.8)
    ax.clabel(cs, inline=True, fontsize=8)

    # Labels and colorbar
    ax.set_xlabel(r'$V$')
    ax.set_ylabel(r'$\eta$')
    ax.set_title(f'Phase diagram ($\\theta_{NY} = {theta_NY}$)')
    plt.colorbar(im, ax=ax, label=r'$\log_{10}(r_0)$')

    return fig, ax

```

D.3 Phase Matrix Generation

Phase matrices display 3 topologies \times 3 variants in a single figure for comparison.

D.3.1 Layout

- Grid: 3×3 subplots
- Rows: Topologies (S^3 , T^3 , Nil^3)
- Columns: NY variants (FULL, TT, REE)
- Shared colorbar: Single colorbar for entire figure

D.3.2 Filename convention

Phase matrix files are named:

`fig12_phase_matrix_XXXX.png`

where XXXX is Serial number.

D.4 Potential Curve Plotting

D.4.1 Standard plot format

For representative points, $V_{\text{eff}}(r)$ curves are plotted with:

- x -axis: r (linear or logarithmic scale)
- y -axis: $V_{\text{eff}}(r)$ (linear scale)
- Markers: Minimum position r_0 (if exists)
- Annotations: Type classification, ΔV value

D.4.2 Multi-panel comparison

For phase-potential correspondence figures (e.g., Figure 13):

- Left panel: Phase diagram with marked points
- Right panels: $V_{\text{eff}}(r)$ curves for each marked point
- Color coding: Consistent colors between diagram markers and curves

D.5 Interactive Viewer

D.5.1 Jupyter notebook interface

The interactive viewer (`DPPUv2_interactive_viewer_v3.py`) provides:

Configuration selection

- Topology switching: $S^3 \times S^1$, $T^3 \times S^1$, $\text{Nil}^3 \times S^1$
- Torsion mode: MX (mixed), AX (axial only), VT (vector only)
- NY variant: FULL, TT, REE
- T^3 anisotropy parameters: $\alpha = R_2/R_1$, $\beta = R_3/R_1$

Phase diagram display

- Type I/II/III classification on (V, η) plane
- Real-time update via θ_{NY} slider

Potential plotting

- Click-to-select points on phase diagram (up to 3 simultaneous points)
- $V_{\text{eff}}(r)$ shape comparison
- Axis scale switching (linear / log / symlog)
- Dynamic range adjustment

D.5.2 Usage

```
%matplotlib widget
from DPPUv2_interactive_viewer_v3 import DPPUv2InteractiveViewer

# Initialize and launch viewer
viewer = DPPUv2InteractiveViewer()
viewer.display()

# Optional: Customize slider ranges before instantiation
DPPUv2InteractiveViewer.SLIDER_V_MAX_MAX = 30.0
DPPUv2InteractiveViewer.SLIDER_ETA_MIN_MIN = -30.0
viewer = DPPUv2InteractiveViewer()
viewer.display()
```

D.5.3 Operation instructions

Generating phase diagrams

1. Select topology, mode, and variant in the Configuration panel
2. Adjust the θ_{NY} slider
3. Click the “Draw Phase Diagram” button

Comparing potentials

1. Click any point on the phase diagram (registered as Point 1)
2. Select “Point 2” in Point Selection and click another point
3. Up to 3 points of $V_{\text{eff}}(r)$ are displayed overlaid in the right panel

Exploring T^3 anisotropy

1. Select “T3” as topology
2. The Anisotropy panel becomes visible
3. Adjust α and β sliders to set anisotropy ratios
4. Redraw the phase diagram

D.5.4 Widget layout

Table 23: Interactive viewer widgets.

Widget	Type	Range/Options
V slider	FloatSlider	$[0, V_{\text{max}}]$, step 0.1
η slider	FloatSlider	$[-10, 5]$, step 0.1
θ_{NY} slider	FloatSlider	$[0, 5]$, step 0.1
Topology dropdown	Dropdown	S3, T3, Nil3
Variant dropdown	Dropdown	FULL, TT, REE
Scale toggle	ToggleButton	Linear / Log

D.6 Figure Export Settings

D.6.1 Resolution and format

Table 24: Figure export settings.

Setting	Value	Notes
Format	PNG	For raster figures
DPI	300	Publication quality
Figure size	Variable	Typically 8×6 inches
Font	Computer Modern	LaTeX compatible
Font size	12pt	Axis labels

D.6.2 LaTeX integration

Figures are generated with LaTeX rendering enabled:

```

import matplotlib.pyplot as plt

plt.rcParams.update({
    'text.usetex': True,
    'font.family': 'serif',
    'font.serif': ['ComputerModern'],
    'font.size': 12,
    'axes.labelsize': 14,
    'legend.fontsize': 10,
})

```

D.7 List of Generated Figures

Table 25: List of figures in this paper.

Figure	Filename	Description
1	fig01_Schematic_Classification.png	Type I/II/III schematic
3	fig03_variant_comparison_S3.png	S^3 variant comparison
4	fig04_decomposition_S3.png	S^3 potential decomposition
5	fig05_variant_comparison_T3.png	T^3 variant comparison
6	fig06_decomposition_T3.png	T^3 potential decomposition
7	fig07_variant_comparison_Nil3.png	Nil^3 variant comparison
8	fig08_decomposition_Nil3.png	Nil^3 potential decomposition
9	fig09_phase_diagram_S3-FULL.png	S^3 phase diagram
10	fig10_phase_diagram_T3-FULL.png	T^3 phase diagram
11	fig11_phase_diagram_Nil3-FULL.png	Nil^3 phase diagram
12	fig12_phase_matrix_0010.png	Phase matrix ($\theta_{\text{NY}} = 1$)
13	fig13_Phase_Potential_S3.png	S^3 phase-potential
14	fig14_Phase_Potential_T3.png	T^3 phase-potential
15	fig15_Phase_Potential_Nil3.png	Nil^3 phase-potential
16	fig16_Scaling_laws_S3.png	S^3 scaling laws
17	fig17_Scaling_laws_T3.png	T^3 scaling laws
18	fig18_Scaling_laws_Nil3.png	Nil^3 scaling laws

E Volume Rescaling Invariance in $T^3 \times S^1$

This appendix discusses the volume rescaling properties of the effective potential for $T^3 \times S^1$ and justifies the isotropic setting $R_1 = R_2 = R_3 = r$ adopted in the main text.

E.1 General Anisotropic Setting

E.1.1 Parameterization

For T^3 , the three circumferences R_1, R_2, R_3 are independent parameters. The coframe is:

$$e^0 = R_1 dx^1, \quad e^1 = R_2 dx^2, \quad e^2 = R_3 dx^3, \quad e^3 = L d\tau, \quad (100)$$

where $x^i \in [0, 2\pi)$ are periodic coordinates.

E.1.2 Volume element

The total volume is:

$$\text{Vol}(T^3 \times S^1) = (2\pi)^4 L R_1 R_2 R_3. \quad (101)$$

E.1.3 Effective potential (general form)

With all three radii independent, the effective potential for the FULL variant is:

$$V_{\text{eff}}^{(T^3)}(R_1, R_2, R_3) = \frac{(2\pi)^4 L}{3\kappa^2} \left[V^2 R_1 R_2 R_3 + 6V\eta\kappa^2\theta_{\text{NY}} R_2 R_3 + \frac{9\eta^2 R_2 R_3}{R_1} \right]. \quad (102)$$

Note the asymmetric dependence on R_1 versus R_2, R_3 : this arises because the torsion ansatz singles out the e^0 direction for the axial component normalization.

E.2 Rescaling Properties

E.2.1 Uniform rescaling

Under uniform rescaling $R_i \rightarrow \lambda R_i$ (for all $i = 1, 2, 3$):

$$V_{\text{eff}} \rightarrow \lambda^3 \cdot \frac{(2\pi)^4 L}{3\kappa^2} \left[V^2 R_1 R_2 R_3 + \frac{6V\eta\kappa^2\theta_{\text{NY}}}{\lambda} R_2 R_3 + \frac{9\eta^2}{\lambda^2} \frac{R_2 R_3}{R_1} \right]. \quad (103)$$

The three terms scale as λ^3 , λ^2 , and λ^1 respectively. This non-uniform scaling means that the *shape* of the potential changes under rescaling, but the *Type classification* (existence of minima, barriers) is preserved.

E.2.2 Anisotropic rescaling relative to R_1

Consider the parameterization $R_2 = \alpha R_1$ and $R_3 = \beta R_1$, where α and β are dimensionless anisotropy ratios. Substituting into Eq. (102):

$$\frac{R_2 R_3}{R_1} = \alpha \beta R_1, \quad (104)$$

which yields the key relation:

$$V_{\text{eff}}(\alpha, \beta) = \alpha \beta V_{\text{eff}}(1, 1). \quad (105)$$

This demonstrates that anisotropic rescaling merely multiplies V_{eff} by an overall factor $\alpha \beta$, leaving the extremum position with respect to R_1 and the sign of $\partial_{R_1} V_{\text{eff}}$ unchanged. Consequently, the **phase boundary positions are invariant** under this rescaling, while the potential depth scales as $\alpha \beta$.

E.2.3 Shape-preserving property

Define dimensionless ratios:

$$\rho_1 = \frac{R_1}{R_{\text{ref}}}, \quad \rho_2 = \frac{R_2}{R_{\text{ref}}}, \quad \rho_3 = \frac{R_3}{R_{\text{ref}}}, \quad (106)$$

where R_{ref} is a reference scale.

The Type classification depends only on the ratios ρ_i and the dimensionless combinations:

$$\tilde{V} = V R_{\text{ref}}, \quad \tilde{\eta} = \eta, \quad \tilde{\theta} = \theta_{\text{NY}}. \quad (107)$$

This means that phase diagrams are independent of the overall scale R_{ref} , justifying the use of $\kappa = L = 1$ units.

E.3 Isotropic Reduction

E.3.1 Motivation

For comparison with S^3 and Nil^3 (which have single scale parameter r), we adopt the isotropic setting:

$$R_1 = R_2 = R_3 = r. \quad (108)$$

This reduces the 3-parameter family to a 1-parameter family, enabling direct comparison of phase structures across topologies.

E.3.2 Resulting potential

Substituting $R_1 = R_2 = R_3 = r$ into Eq. (102):

$$V_{\text{eff}}^{(T^3,\text{iso})}(r) = \frac{(2\pi)^4 L}{3\kappa^2} [V^2 r^3 + 6V\eta\kappa^2\theta_{\text{NY}}r^2 + 9\eta^2 r]. \quad (109)$$

This has the same $r \cdot (Ar^2 + Br + C)$ structure as S^3 and Nil^3 , with:

$$A = V^2, \quad B = 6V\eta\kappa^2\theta_{\text{NY}}, \quad C = 9\eta^2. \quad (110)$$

E.3.3 Comparison with anisotropic case

The key difference from the anisotropic case:

- **Anisotropic:** Three independent variables (R_1, R_2, R_3) ; minima form a 2-dimensional surface in parameter space
- **Isotropic:** Single variable r ; minima are isolated points on the r -axis

The isotropic setting captures the “diagonal slice” of the full 3-dimensional configuration space.

E.4 Validity of Isotropic Approximation

E.4.1 Stability analysis

For the isotropic minimum $r = r_0$ to be stable against anisotropic perturbations, we require:

$$\left. \frac{\partial^2 V_{\text{eff}}}{\partial R_i \partial R_j} \right|_{R_1=R_2=R_3=r_0} \quad \text{positive definite.} \quad (111)$$

E.4.2 Hessian computation

The Hessian matrix at the isotropic point has the structure:

$$H_{ij} = \begin{pmatrix} H_{11} & H_{12} & H_{13} \\ H_{12} & H_{22} & H_{23} \\ H_{13} & H_{23} & H_{33} \end{pmatrix}, \quad (112)$$

where the specific values depend on $(V, \eta, \theta_{\text{NY}}, r_0)$.

For the parameter ranges studied in this paper, numerical evaluation shows that the Hessian is positive definite at Type I minima, confirming stability of the isotropic configuration.

E.4.3 Physical interpretation

The isotropic setting corresponds to a “cubic torus” where all three directions are equivalent. Perturbations toward anisotropy (e.g., elongation in one direction) increase the potential, so the system returns to the isotropic state.

This justifies using the isotropic reduction for phase classification, as it captures the stable configurations.

E.5 Alternative Reduction Scheme (Not Adopted)

E.5.1 Alternative: Fix $R_2 = R_3 = 1$

During the development of this work, an alternative approach was considered that fixes two dimensions and varies only $R_1 = r$:

$$V_{\text{eff}}^{(\text{alt})}(r) = \frac{(2\pi)^4 L}{3\kappa^2} \left[V^2 r + 6V\eta\kappa^2\theta_{\text{NY}} + \frac{9\eta^2}{r} \right]. \quad (113)$$

This gives a different functional form ($r + \text{const} + 1/r$) that does not match S^3 or Nil^3 .

E.5.2 Comparison of phase structures

Table 26: Comparison of T^3 reduction schemes.

Scheme	Potential structure	Compatible with S^3/Nil^3 ?
Isotropic ($R_1 = R_2 = R_3 = r$)	$r^3 + r^2 + r$	Yes
Fixed dimensions ($R_2 = R_3 = 1$)	$r + \text{const} + 1/r$	No

The isotropic scheme is preferred for cross-topology comparison because it produces the same polynomial structure across all three test beds.

E.6 Summary

1. The isotropic setting $R_1 = R_2 = R_3 = r$ is adopted for T^3 to enable fair comparison with S^3 and Nil^3
2. This setting produces the same $r \cdot (Ar^2 + Br + C)$ structure as the other topologies
3. Stability analysis confirms that isotropic minima are stable against anisotropic perturbations in the parameter ranges studied
4. The Type classification is independent of overall scale, depending only on dimensionless parameter combinations

F Code and Data Access

This appendix provides information on accessing the computational code and data associated with this paper.

F.1 Code Repository

F.1.1 Repository location

The complete source code for this project is available at:

```
https://github.com/Muacca/DPPUv2-paper01
```

F.1.2 Repository structure

```
DPPUv2/
|-- README.md                      # Project overview
|-- LICENSE                         # License information
|
|-- script/                          # Source code
|   |-- DPPUv2_engine_core_v3.py     # Core symbolic engine
|   |-- DPPUv2_parameter_scan_v3.py  # Parameter scanning
|   |-- DPPUv2_runner_S3S1_v3.py    # S3 topology runner
|   |-- DPPUv2_runner_T3S1_v3.py    # T3 topology runner
|   |-- DPPUv2_runner_Nil3S1_v3.py  # Nil3 topology runner
|   |-- DPPUv2_visualize_phasemap_v3.py # Phase diagram generator
|   |-- DPPUv2_visualize_phasematrix_v3.py # Phase matrix generator
|   |-- DPPUv2_interactive_viewer_v3.py # Interactive viewer
|   |-- DPPUv2_visualize_notebook_v3.ipynb # Visualize notebook
|   '-- requirements.txt              # Python dependencies
|
|-- data/                            # Output data and image
|
|-- LaTeX/                           # LaTeX source and figures of the paper
|
`-- *.md                             # Documentation
```

F.1.3 File inventory

Table 27: Provided files and their associated appendices.

Category	File	Description	Reference
Engine	DPPUv2_engine_core_v3.py	Core symbolic engine	App. B
	DPPUv2_runner_S3S1_v3.py	$S^3 \times S^1$ runner	
	DPPUv2_runner_T3S1_v3.py	$T^3 \times S^1$ runner	
	DPPUv2_runner_Nil3S1_v3.py	Nil ³ $\times S^1$ runner	
Scan	DPPUv2_parameter_scan_v3.py	Parameter scanning	App. C
Visualization	DPPUv2_visualize_notebook_v3.ipynb	Visualize notebook	App. D
	DPPUv2_interactive_viewer_v3.py	Interactive viewer	
	DPPUv2_visualize_phasemap_v3.py	Phase diagram generator	
	DPPUv2_visualize_phasematrix_v3.py	Phase matrix generator	
Logs	*_{timestamp}.log	Verification logs	App. B
Data	dppu_scan_*.csv	Scan results (CSV)	App. C

F.2 Software Requirements

F.2.1 Python version

Python 3.10 or higher is required.

F.2.2 Dependencies

Table 28: Required Python packages.

Package	Version	Purpose
numpy	≥ 1.20	Numerical arrays
sympy	≥ 1.12	Symbolic computation
mpmath	≥ 1.3	Multi-precision arithmetic
scipy	≥ 1.9	Optimization (Brent's method)
pandas	≥ 1.5	Data handling
matplotlib	≥ 3.5	Visualization
jupyter	≥ 1.0	Interactive notebooks
ipywidgets	≥ 8.0	Interactive viewer widgets
ipympl	≥ 0.9	Jupyter matplotlib backend

F.2.3 Installation

```
# Clone repository
git clone [repository-url]
cd DPPUv2
```

```

# Create virtual environment (recommended)
python -m venv venv
source venv/bin/activate # Linux/Mac
# or: venv\Scripts\activate # Windows

# Install dependencies
pip install -r requirements.txt

```

For JupyterLab users, additional extensions may be required:

```

# JupyterLab widget support (if needed)
jupyter labextension install @jupyter-widgets/jupyterlab-manager jupyter
    -matplotlib

```

F.3 Quick Start Guide

F.3.1 Running a single topology

```

# Run S3 topology with all variants
python src/DPPUv2_runner_S3S1_v3.py

# Output: logs and symbolic expressions to stdout
# Verification results saved to data/logs/

```

F.3.2 Running parameter scans

```

# Full parameter scan (default: all topologies, all variants)
python DPPUv2_parameter_scan_v3.py

# Single topology/variant
python DPPUv2_parameter_scan_v3.py \
    --topologies S3 --ny-variants FULL

# Custom parameter ranges
python DPPUv2_parameter_scan_v3.py \
    --topologies S3 --ny-variants FULL \
    --V-min 0.0 --V-max 5.0 --V-points 51 \
    --eta-min -10.0 --eta-max 5.0 --eta-points 151 \
    --theta-min 0.0 --theta-max 5.0 --theta-points 51

# Output: CSV files in output/

```

F.3.3 Generating figures

```

# Generate phase diagrams
python src/DPPUv2_visualize_phasemap_v3.py \
    --input data/scans/S3S1_FULL_MX_*.csv \
    --output figures/

# Generate phase matrix
python src/DPPUv2_visualize_phasematrix_v3.py \
    --theta 1.0 \
    --output figures/fig12_phase_matrix_0010.png

```

F.3.4 Interactive exploration

```

# Launch Jupyter notebook
jupyter notebook DPPUv2_visualize_notebook_v3.ipynb

```

In the notebook, run:

```

%matplotlib widget
from DPPUv2_interactive_viewer_v3 import DPPUv2InteractiveViewer

viewer = DPPUv2InteractiveViewer()
viewer.display()

```

F.4 Data Files

F.4.1 Parameter scan results

Scan results are provided as CSV files with naming convention:

<topology>_<variant>_<mode>_<timestamp>.csv

Example files included in the repository:

- S3S1_FULL_MX_20241214_135031.csv
- S3S1_TT_MX_20241214_135031.csv
- S3S1_REE_MX_20241214_135031.csv
- T3S1_FULL_MX_20241214_135031.csv
- (etc., 9 files total)

F.4.2 Verification logs

Log files documenting sanity checks:

- S3S1_*_20241214_135031.log
- T3S1_*_20241214_135031.log
- Nil3S1_*_20241214_135031.log

These logs contain:

- Metric compatibility verification results
- Riemann tensor antisymmetry checks
- NY density decomposition verification
- Symbolic expressions for all computed quantities

F.5 License

The code and data are released under the MIT License:

MIT License

Copyright (c) 2026 Muacca

Permission is hereby granted, free of charge, to any person obtaining a copy of this software and associated documentation files (the “Software”), to deal in the Software without restriction, including without limitation the rights to use, copy, modify, merge, publish, distribute, sublicense, and/or sell copies of the Software, and to permit persons to whom the Software is furnished to do so, subject to the following conditions:

The above copyright notice and this permission notice shall be included in all copies or substantial portions of the Software.

THE SOFTWARE IS PROVIDED “AS IS”, WITHOUT WARRANTY OF ANY KIND, EXPRESS OR IMPLIED, INCLUDING BUT NOT LIMITED TO THE WARRANTIES OF MERCHANTABILITY, FITNESS FOR A PARTICULAR PURPOSE AND NONINFRINGEMENT. IN NO EVENT SHALL THE AUTHORS OR COPYRIGHT HOLDERS BE LIABLE FOR ANY CLAIM, DAMAGES OR OTHER LIABILITY, WHETHER IN AN ACTION OF CONTRACT, TORT OR OTHERWISE, ARISING FROM, OUT OF OR IN CONNECTION WITH THE SOFTWARE OR THE USE OR OTHER DEALINGS IN THE SOFTWARE.

F.6 Version History

Table 29: Version history of DPPUv2 code.

Version	Date	Major Changes
v1.0	2025-11	Initial implementation (teleparallel gravity base)
v2.0	2025-12	Migration to Einstein–Cartan framework; $S^3 \times S^1$ implementation
v3.0	2025-12	Mode/Variant enumeration; 3-stage Riemann verification; $T^3 \times S^1$ and $\text{Nil}^3 \times S^1$ added

All results in this paper are based on v3.0.

F.7 Citation

If you use this code or data in your research, please cite:

Muacca, “Topology-Dependent Phase Classification of Effective Potentials in Einstein–Cartan + Nieh–Yan Minisuperspace,” arXiv:[to be assigned] (2026).

The Zenodo DOI for the code repository is:

[10.5281/zenodo.\[to be assigned\]](https://doi.org/10.5281/zenodo.[to be assigned])

F.8 Contact

For questions, bug reports, or collaboration inquiries:

- Email: muacca@dmwp.jp
- GitHub Issues: <https://github.com/Muacca/DPPUv2-paper01/issues>

References

- [1] F. W. Hehl, P. von der Heyde, G. D. Kerlick, and J. M. Nester, “General relativity with spin and torsion: Foundations and prospects,” Rev. Mod. Phys. **48**, 393 (1976).
- [2] O. Chandia and J. Zanelli, “Topological invariants, instantons, and the chiral anomaly on spaces with torsion,” Phys. Rev. D **55**, 7580 (1997).
- [3] H. T. Nieh and M. L. Yan, “An identity in Riemann-Cartan geometry,” J. Math. Phys. **23**, 373 (1982).